ATOMIC DIFFUSION IN THE URANIUM-50WT% ZIRCONIUM NUCLEAR FUEL SYSTEM

A Thesis

by

DANIEL R. EICHEL

Submitted to the Office of Graduate Studies of
Texas A&M University
in partial fulfillment of the requirements for the degree of

MASTER OF SCIENCE

Chair of Committee,	Sean McDeavitt
Committee Members,	Lin Shao
	Xinghang Zhang
Head of Department,	Yassin Hassan

August 2013

Major Subject: Nuclear Engineering

ABSTRACT

Atomic diffusion phenomena were examined in a metal-alloy nuclear fuel system composed of δ-phase U-50wt%Zr fuel in contact with either Zr-10wt%Gd or Zr-10wt%Er. Each alloy was fabricated from elemental feed material via melt-casting, and diffusion samples of nominal 1.5 mm thickness were prepared from the resulting alloy slugs. The samples were assembled into diffusion couples and annealed for periods of 14, 28, and 56 days at temperatures of 550°C, 600°C, and 650°C. Thus, the U-50Zr/Zr-10Er system and the U-50Zr/Zr-10Gd system were each annealed for three different time periods at each of three different temperatures, for an initial total of 18 diffusion interfaces that were to be studied. In practice, data was collected from only 12 of the 18 interfaces. At 650°C, the U-50wt%Zr alloy exists in the γ-phase region, which enabled the comparison of diffusion behavior between the δ phase and γ phase.

Diffusion samples were examined by collecting composition profiles across the diffusion interface for each element via electron probe microanalysis. From the resulting experimental data diffusion coefficients were evaluated. Diffusion coefficients were found to be on the order of 10^{-19} m^2/s in the δ-phase systems, and 10^{-17} m^2/s in the γ-phase systems.

It was observed that atomic mobility of all diffusing species was generally greater in the U-50Zr/Zr-10Gd system than in the U-50Zr/Zr-10Er system; furthermore, it was found that diffusion rates were considerably higher above the phase transformation temperature into the γ phase, as indeed would be expected in the more

open structure of the body-centered cubic γ phase, as compared to the hexagonal δ-phase U-Zr. However, values for diffusion coefficients measured in this study were considerably smaller than those found in past studies of δ-phase U-Zr, which are on the order of 10^{-17} m^2/s. It is likely that diffusion was inhibited by the formation of stable metal oxides resulting from oxygen contamination; it is also possible that diffusion was suppressed by the presence of the erbium and gadolinium.

ACKNOWLEDGEMENTS

I would like to thank my advisor, Dr. Sean McDeavitt, as well as the other members of my graduate committee, Dr. Lin Shao and Dr. Xinghang Zhang, for their guidance and expertise over the course of this study. I would also like to thank Aaron Totemeier and Lightbridge Corporation for their involvement in this study.

I would like to thank Grant Helmreich for sharing the knowledge and experience he gained through his own diffusion couple studies, and his willingness to provide assistance in mine.

I also wish to thank Adam Parkison for his guidance and mentorship throughout the years that I have been involved with the Fuel Cycle and Materials Laboratory, both when I was an undergraduate student technician as well during my graduate research.

I would like to thank Dr. Ray Guillemette and the Electron Microprobe Lab in the Department of Geology at Texas A&M University. Dr. Guillemette's assistance and expertise helped me to understand the theory and methods of electron probe microanalysis and their application to my studies.

I would also like to acknowledge the machine shop in the Department of Nuclear Engineering at Texas A&M University, which was instrumental in the fabrication of custom parts for my experimental apparatuses.

NOMENCLATURE

A-xxB	Binary metal alloy consisting principally of component *A* with the inclusion of *xx* weight % component *B* (example: Zr-10Gd)
BCC	Body-centered cubic (crystal structure)
BSE	Backscatter electron (imaging method)
CTE	Coefficient of thermal expansion (linear)
D	Diffusion coefficient [m^2/s]
E	Young's Modulus / Elastic Modulus [Pa]
EDS	Energy dispersive spectroscopy
EES	Engineering Equation Solver (software package)
EPMA	Electron probe microanalysis
FCML	Fuel Cycles and Materials Laboratory
FGR	Fission gas release
HCP	Hexagonal close-packed (crystal structure)
Lα , Mα	Nomenclature for atomic electron transition and emission of associated characteristic x-ray
LIF	Lithium Fluoride (diffracting crystal)
LWR	Light water reactor
MRF	Materials Research Furnace

*N*wk###	Diffusion sample labeling nomenclature, in which *N* is the number of weeks in the annealing time and ### is the temperature in °C (example: 2wk550)
PET	Pentaerythritol (diffracting crystal)
SE	Secondary electron (imaging method)
WDS	Wavelength dispersive spectroscopy

TABLE OF CONTENTS

Page

LIST OF FIGURES

Page

LIST OF TABLES

Page

1. INTRODUCTION

1.1. Overview

In this work, a study was carried out to examine diffusion phenomena that may be relevant to the performance of components of a metallic nuclear fuel system under development by Lightbridge Corporation (address: Maclean, VA). A cross section of this fuel system, depicted below in Figure 1, consists of a U-50Zr alloy fuel region (all compositions in this document are presented in wt%), as well as an unfueled "displacer" region composed mainly of zirconium. Permutations of the fuel design include the presence of burnable absorber elements, namely erbium and gadolinium, in this unfueled displacer region. In nuclear fuel systems, a burnable absorber is a species that strongly absorbs neutrons, and in so doing is transmuted to another species that does not strongly absorb neutrons. The inclusion of such an absorber in a nuclear fuel initially decreases the reactivity of the fuel, but this effect diminishes over time as the absorber is burned out; thus, a burnable absorber. Due to the negative reactivity contribution of the burnable absorbers, fresh fuel can safely include more fissile material, thereby increasing the fuel lifetime in the core. As part of the verification process of the Lightbridge fuel concept, this study examined the diffusion phenomena between the U-50Zr material and two candidate burnable absorber alloys: Zr-10Gd and Zr-10Er. This study was carried out in the Fuel Cycles and Materials Laboratory (FCML) in the Department of Nuclear Engineering at Texas A&M University.

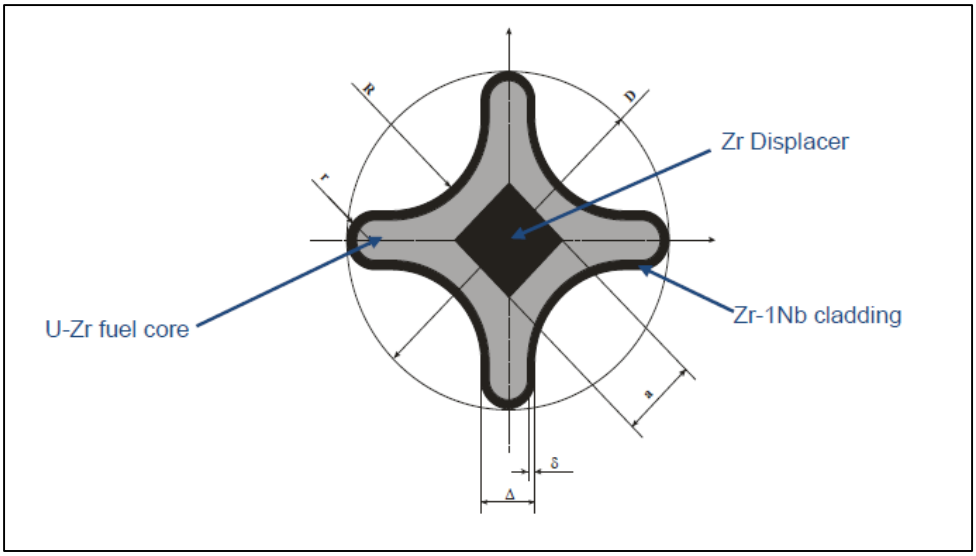

Figure 1: Cross section of a nuclear fuel rod according to the Lightbridge design concept. Image courtesy Lightbridge Corporation.

The fuel alloy composition of U-50Zr was selected for this nuclear fuel design because this particular alloy exists as the UZr_2 δ-phase structure below 600°C, as can be seen in the phase diagram shown in Figure 2. This phase is known to be very stable, and past studies (Ogawa, et al., June 1998) have demonstrated that this material is expected to exhibit very little fission gas release or volumetric swelling induced by irradiation. Similarly, it is also expected that diffusion rates will be very low in this δ-phase system due to its stability, as will be discussed in Section 2.2. Therefore, it is not expected that the effects of diffusion behavior will be a limiting factor in the performance of this fuel design. This study intended to verify this expectation through the experimental quantification of the parameters that govern atomic diffusion in this system.

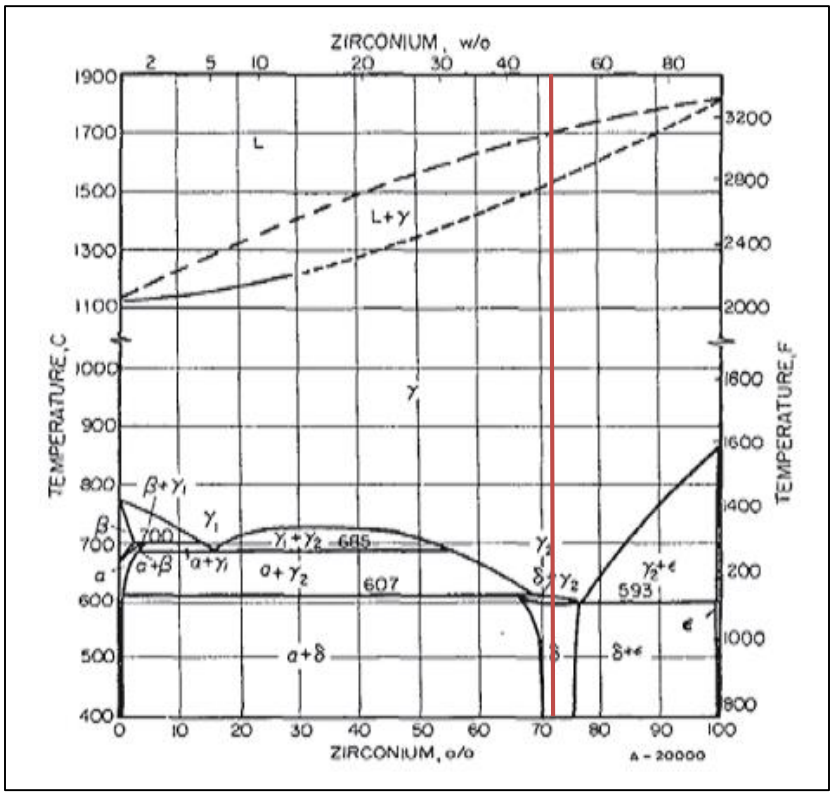

Figure 2: Phase diagram for the binary zirconium-uranium system, showing the existence of the δ phase below 600°C for alloy compositions in the neighborhood of U-50wt%Zr (U-72at%Zr). Graphic adopted from (Akabori, Itoh, Ogawa, Kobayashi, & Suzuki, Stability and Structure of the Delta Phase of the U-Zr Alloys, June 1992).

1.2. The Lightbridge Fuel Concept

The objective of the Lightbridge fuel design is to develop a high-thermal-conductivity alternative to the uranium dioxide (UO_2) ceramic fuel form currently in use in light water reactor (LWR) systems. While UO_2 has many attractive properties as a nuclear fuel, its greatest shortcoming is its very low thermal conductivity; as a result, the fuel operates at high temperature and it requires a large amount of time to remove

residual heat from the fuel after reactor shutdown. This can be a particularly salient factor if there is a loss of core cooling in an accident scenario.

Consequently, there is great incentive for high-thermal-conductivity fuel forms to be developed. In general, metal alloy fuels exhibit very good thermal properties; however, irradiation of metallic fuels is generally accompanied by very severe volumetric swelling and large releases of fission gases. It is in these respects that the U-50Zr alloy is an exception; this alloy does not seem to share the shortcomings of other metal fuel forms. In a study carried out by Ogawa, et al, (Ogawa, et al., June 1998) δ-phase U-Zr alloy was shown to exhibit very little volumetric swelling and fission gas release, as compared to other U-Zr phases. Quantitative findings of this study are tabulated below in Table 1, with the final row of data (Sample Zr1) corresponding to the δ-phase sample.

Table 1: Fission gas release (FGR) and volumetric swelling data for various U-Zr alloys irradiated at approximately 600°C. Data from (Ogawa, et al., June 1998).

Sample	at% Zr	FGR (%)	ΔV/V (%)
Zr12	30	7.7	40
Zr14	30	7.2	46
Zr6	10	9.7	61
Zr7	30	12.5	67
Zr10	30	10.5	42
Zr5	10	15.7	*
Zr1	70	0.02	3

*data unavailable

Clearly, the degrees of fission gas release and volumetric swelling in the δ-phase sample are significantly below those exhibited by other U-Zr compositions. Thus, the utilization of δ-phase U-50Zr allows for the development of a high-thermal-conductivity nuclear fuel form that operates at low temperature (below 600°C) and from which residual heat can be removed very readily. The adoption of such a fuel form in commercial LWR systems would allow for increased safety margins and decrease the probability of severe accidents due to insufficient fuel cooling.

2. BACKGROUND

2.1. Fundamental Diffusion Phenomenology

At the interface between the fuel material and the central displacer in the Lightbridge fuel design, dissimilar alloys are in direct contact with one other. At the operating temperature of the fuel random atomic motion will induce species from either side of the interface to diffuse into one another. Fick's Second Law provides a general description of the behavior of time-dependent, solid-state diffusion driven by a concentration gradient:

$$\boxed{\frac{\partial C}{\partial t} = D\frac{\partial^2 C}{\partial x^2}} \qquad \text{Equation 1}$$

where C is the concentration of the species in question, t is time, x is the diffusion distance, and D is the diffusion coefficient, particular to the system in question and the temperature.

If the mass flux of species diffusing across the interface in either direction is unequal, as is usually the case, a phenomenon called the Kirkendall Effect (Borg & Dienes, 1988) is observed. As shown schematically in Figure 3 below, unequal fluxes (denoted by the letter "J") result in a net displacement of the interface.

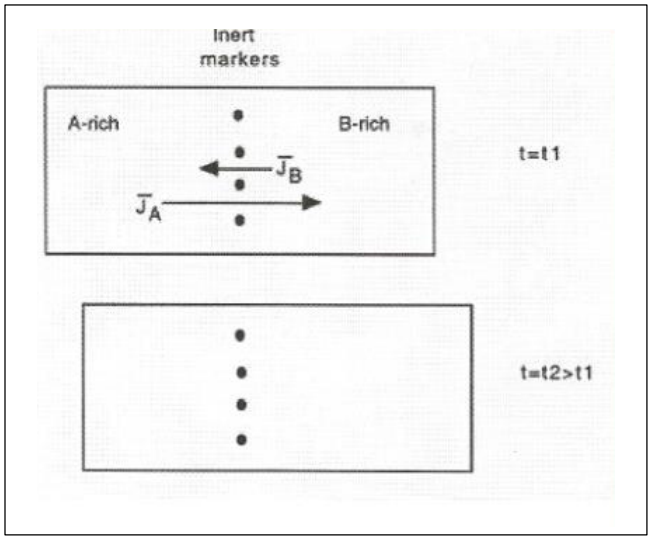

Figure 3: Simple schematic representation of the Kirkendall Effect, in which the location of a material interface is displaced due to unequal diffusion fluxes across it. Graphic adopted from (Borg & Dienes, 1988).

Another fundamental concept in diffusion phenomena involves the existence of a conservation of mass plane for a given constituent in a system. At the location of this conservation plane, called the Matano plane, the material loss on one side is equal to the material gain on the other side, as is shown graphically in Figure 4. The Matano plane is an important tool in quantifying diffusion coefficients, as will be discussed more fully in Section 3.5.3 of this document. Due to the Kirkendall Effect, the location of the Matano plane for a given constituent is seldom, if ever, consist with that of another constituent or the original interface.

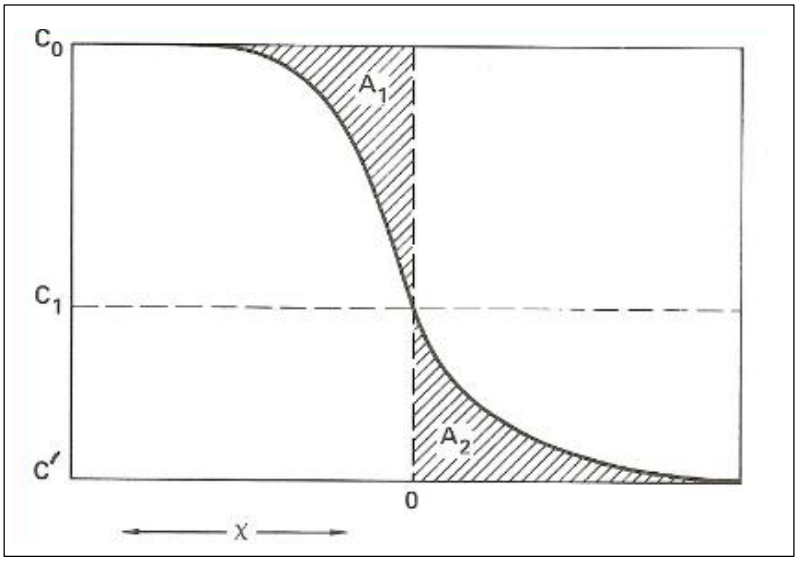

Figure 4: Graphical representation of the Matano plane for an arbitrary composition profile. By the definition of the Matano plane, $A_1 = A_2$.
Graphic adopted from (Borg & Dienes, 1988).

As a result of these phenomena, it is necessary to carry out a study of diffusion behavior as part of the verification process of the Lightbridge fuel design. Before this fuel could be put into service it is necessary to understand how the material composition and structure will be changing at the fuel/displacer interface during service. Diffusion phenomena will induce the creation of different composition regions at the interface, introducing the presence of different structures and phases not present in the original fuel system. These regions will likely exhibit varying neutronic, mechanical, chemical, and thermal properties that could lead to potential failure mechanisms. It is necessary to be able to anticipate such possible failure modes in order to determine whether diffusion behavior could be a limiting factor in the service lifetime of this fuel form.

2.2. Literature Review

In conducting a literature review prior to this work, no study was found that examines diffusion phenomena between the particular aforementioned alloys; this was no great surprise, due to the unique nature of the Lightbridge fuel system. There have, however, been other studies that examine diffusion in U-Zr alloys, including δ-phase U-Zr, most notably a study carried out by Akabori, et al (Akabori, Itoh, Ogawa, & Ogata, Interdiffusion in the U-Zr System at Delta-Phase Compositions, June 1998). While the work by Akabori, et al does not include the burnable absorber alloys, it did provide pertinent information regarding diffusion characteristics of δ-phase U-Zr. Diffusion coefficients, denoted by the letter *D*, were evaluated for diffusion couples assembled with U-Zr alloys of slightly different composition (about 7-10 at%), but that still fell within the same phase region. These values can be found below in Table 2, and are plotted in Figure 5 as well. This figure also provides a comparison between the data found by Akabori, et al and that found in another study carried out by Ogata, et al (Ogata, Akabori, Itoh, & Ogawa, June 1996).

Table 2: Values of the diffusion coefficient measured in U-Zr; data from (Akabori, Itoh, Ogawa, & Ogata, Interdiffusion in the U-Zr System at Delta-Phase Compositions, June 1998).

Diffusion Couple [at%]	Temperature [C]	Phase	D [m^2/s]
U-68Zr/U-75Zr	550	δ	0.49×10^{-17}
U-67Zr/U-75Zr	580	δ	1.22×10^{-17}
U-68Zr/U-75Zr	650	γ	38.3×10^{-17}
U-68Zr/U-78Zr	700	γ	117×10^{-17}
U-68Zr/U-78Zr	750	γ	177×10^{-17}

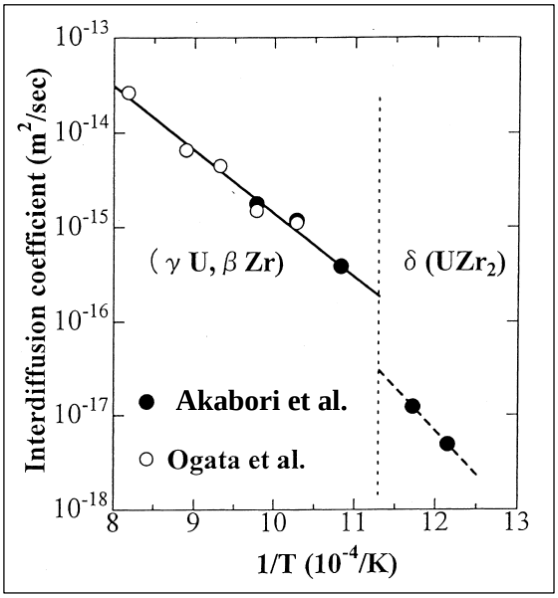

Figure 5: Arrhenius plot providing a comparison of diffusion coefficient values from past studies; data from Akabori, et al is shown in black, while that from Ogata, et al is shown in white. Graphic adopted from (Akabori, Itoh, Ogawa, & Ogata, Interdiffusion in the U-Zr System at Delta-Phase Compositions, June 1998).

Furthermore, this same work by Akabori, et al provided some insight into the expected structure and appearance of a diffusion interface in δ-phase U-Zr. As seen

below in Figure 6, the diffusion interface exhibits a two-phase precipitate structure of light-colored uranium-rich grains as well as dark-colored zirconium-rich grains.

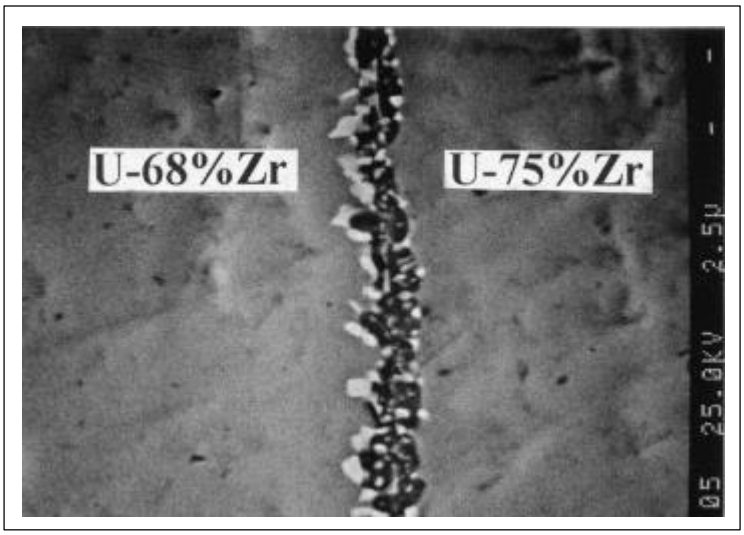

Figure 6: Backscatter electron image of the diffusion zone in U-68at%Zr/U-75at%Zr annealed at 520°C, showing a two-phase precipitate at the interface. Image from (Akabori, Itoh, Ogawa, & Ogata, Interdiffusion in the U-Zr System at Delta-Phase Compositions, June 1998).

However, this structure is somewhat at odds with that predicted by diffusion theory, according to which the reaction zone would be expected to form a multi-layer structure of intermetallic compounds, each with its own discreet composition. This is dictated by the Gibbs Phase Rule, which relates the parameters that govern phase equilibria as follows:

$$\boxed{P + F = C + N} \qquad \text{Equation 2}$$

where, in a given system, *P* is the number of phases present, *F* is the number of degrees of freedom, *C* is the number of chemical components, and *N* is the number of intensive variables, usually temperature and pressure. Thus, in the systems under examination in this study, *P* and *C* were both equal to 3, so there were only two degrees of freedom; once temperature and pressure were selected, there was no additional degree of freedom to allow for varying composition. The diffusion zone would therefore be expected to exhibit a series of layered single-phase regions with discreet compositions. An example of such a layered structure at a diffusion interface is shown below in Figure 7 for a uranium-iron system studied by Huang, et al (Huang, et al., February 2012).

As will be seen later, both the structure shown in Figure 6 and that shown in Figure 7 were in fact observed in this study.

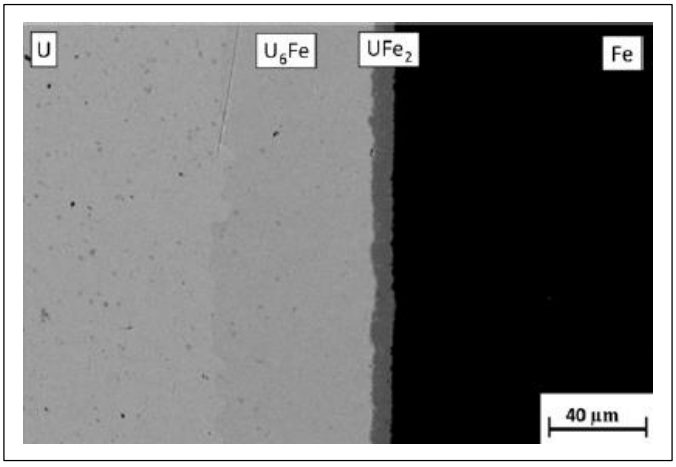

Figure 7: Example of a diffusion interface that exhibits layers of intermetallic regions in a uranium-iron system. Image adopted from (Huang, et al., February 2012).

Literature review also revealed the δ-phase U-Zr alloy to exist in a crystal structure very closely akin to the aluminum diboride (AlB_2) structure (Landa, Soderlind, & Turchi, December 2008). This structure, as seen in Figure 8 below, is similar to the basic hexagonal close-packed (HCP) structure, but with the exception that the middle plane of B atoms includes six atoms, rather than three. This modification allows the unit cell to be collapsed to the simpler unit cell shown in Figure 9 for the U-Zr system. By comparing Figure 8 and Figure 9, it can be seen that in this structure Zr atoms occupy the Al sites, while both U and Zr atoms occupy the B sites; it should be noted that δ-phase U-Zr does not always exist with perfect UZr_2 stoichiometry, and that Zr atoms will occupy the B sites as necessary to accommodate some fluctuation away from the exact 2:1 atom ratio.

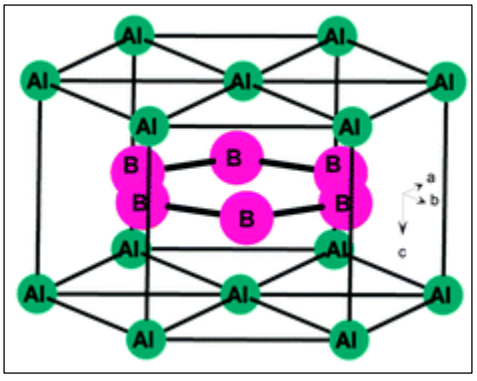

Figure 8: AlB_2 crystal structure. Image adopted from (Callister & Rethwisch, 2008).

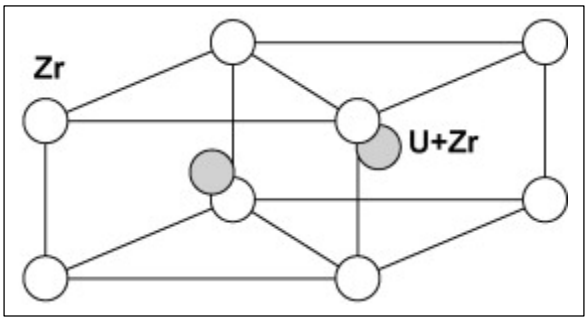

Figure 9: Unit cell for the δ-phase U-Zr crystal structure. Note that both U and Zr atoms occupy the B sites of the AlB_2 structure. Graphic adopted from (Havela, et al., 2008).

3. EXPERIMENTAL METHODS

This work studied the diffusion behavior between the U-50Zr fuel material and two candidate displacer materials, both of which included burnable absorbers: Zr-10Er and Zr-10Gd. Samples of these three alloys were assembled into diffusion couples and annealed for various lengths of time at a series of different temperatures.

3.1. Experimental Matrix and Objectives

Annealing times were selected to be two, four, and eight weeks in duration. Annealing temperatures were selected to be 550°C, 600°C, and 650°C so as to examine the effects of the phase change out of the δ-phase region. Recall from Figure 2 (page 3) that the phase change from the δ phase to the γ phase occurs at an approximate temperature of 600°C, varying slightly depending on the composition. The lowest annealing temperature (550°C) is the expected maximum temperature the fuel will experience in normal operation, but should any temperature excursions ever occur, it is expected that diffusion rates will be much more rapid in the higher-temperature γ-phase region due to the transition from the AlB_2-type δ-phase structure to the much more open body-centered cubic (BCC) γ-phase structure (Akabori, Ogawa, Itoh, & Morii, April 1995). Thus, annealing temperatures in the γ-phase region were included in this study as well, and the three temperatures were selected to fall in the pure δ, δ+γ, and pure γ regions, respectively. However, the longest annealing time (8 weeks) was not carried out at the highest temperature (650°C), as diffusion rates were sufficiently rapid that

such a long anneal was not necessary. This experimental matrix is summarized below in Table 3.

Table 3: Proposed experimental matrix for diffusion annealing.

Annealing Temperature ↓ \ Annealing Time →			
	2 week 550°C	4 week 550°C	8 week 550°C
	2 week 600°C	4 week 600°C	8 week 600°C
	2 week 650°C	4 week 650°C	

This study included four major phases, as follows:

1) **Casting of alloys.** Each of the three alloys included in this study was fabricated from elemental feed material via melt-casting. For the materials in question, this was done using yttria crucibles at a temperature of approximately 1900°C. Homogeneity analysis followed the melt-castings to ensure alloy constituents were sufficiently uniformly distributed.

2) **Assembly of diffusion couples and furnace.** Discs of sample material were cut radially from the as-cast alloy slugs and stacked together in a diffusion couple. A clamping structure, composed of materials with appropriate thermal properties for this application, immobilized the stack of diffusion samples. This apparatus was then annealed in a furnace system equipped to maintain an inert atmosphere of flowing argon.
3) **Diffusion annealing.** The annealing experiments were carried out according to the temperatures and durations specified above.
4) **Interface characterization and data analysis.** Upon completion of diffusion annealing, samples were mounted in epoxy, sectioned, polished, and examined under electron probe microanalysis (EPMA). Using wavelength dispersive spectroscopy (WDS), line scans across the diffusion interfaces were used to acquire quantitative composition profiles, which were then analyzed to evaluate diffusion parameters.

This summarizes the experimental work carried out in this diffusion study. Each of these phases of the project is discussed in detail in Sections 3.2, 3.3, 3.4, and 3.5 of this document, respectively.

The principal objective of this study was to evaluate diffusion coefficients at each of the temperatures considered by collecting elemental composition profiles across the diffusion interface. As discussed in Section 2.2 of this document, it was expected according to past work (Akabori, Itoh, Ogawa, & Ogata, Interdiffusion in the U-Zr System at Delta-Phase Compositions, June 1998) that diffusion rates in δ-phase U-Zr

would be very low, with diffusion coefficients on the order of 10^{-17} m^2/s. Furthermore, as discussed in Section 2.2, it was expected that the diffusion interfaces would form either a two-phase precipitate region similar in appearance to that depicted in Figure 6, or a multi-layered structure of intermetallic compounds similar to that depicted in Figure 7, or perhaps both.

Upon completion of this study, a final objective was the formulation of hypotheses regarding the possible effects of diffusion on fuel performance in actual service. Since diffusion rates were expected to be low, it was not expected that diffusion phenomena would be a limiting factor on fuel lifetime; however, the possibility existed that unexpected surprises could reveal themselves in this study, and all possibilities needed to be considered for the verification of the Lightbridge fuel design.

3.2. Casting of Alloy Samples

The alloys to be studied in this work (U-50Zr, Zr-10Er, and Zr-10Gd) are not alloys that were readily available for purchase; consequently, each of the three alloys needed to be fabricated from elemental feed material. The FCML is equipped with a Materials Research Furnace (MRF) that is capable of reaching the temperatures necessary to fabricate these alloys via melt-casting.

3.2.1. The MRF Furnace

The MRF is a high-temperature furnace capable of heating samples to approximately 2000°C under either inert atmosphere or hard vacuum. The vacuum

system includes both a mechanical roughing pump as well as a turbopump to reach higher vacuum levels. Electrical resistive heating is produced in sets of heating elements composed of a tungsten mesh, and the sample is placed on a tungsten pedestal at the center of the array of heating elements. Heat is confined within the sample chamber by multilayered molybdenum heat shields. Finally, the stainless-steel walls of the hot zone are cooled by a cooling jacket of flowing water, with numerous pass-throughs for instrumentation and the gas inlet and outlet valves for runs under inert atmosphere. Many of these features can be seen in Figure 10 below.

Figure 10: A picture of the MRF, showing the control panel as well as the inside of the open door of the hot zone. The semi-cylindrical set of heating elements and heat shields seen here mates with an identical set in the back of the hot zone when the door is closed.

3.2.2. Preparation of Feed Material

A series of steps were taken to prepare the elemental feed material for casting. Some measures needed to be taken to remove oxidation from the uranium and zirconium stock, although no such measures were necessary for the erbium and gadolinium, as the stock material of these elements arrived packaged under argon and the pieces to be melted were prepared within an argon-atmosphere glovebox. Oxidation was removed from the uranium stock with nitric acid. The zirconium stock available in the FCML was in the form of crystal bars that exhibited very irregular, multifaceted surfaces. This surface irregularity was removed by turning down the bars on a lathe, thereby serving two purposes: this removed the oxidation layer, while at the same time rendered the bar into a regular cylinder, from which it was much easier to calculate and cut the right length so as to produce a piece with the appropriate mass for casting. Figure 11 provides an illustration of the preparation of the zirconium. Finally, pieces of each material were cut and sectioned as necessary in order to attain the correct mass proportions for each alloy to be cast, respectively: U-50Zr, Zr-10Er, and Zr-10Gd.

Figure 11: Comparison of a stock zirconium bar and a segment that has been prepared for casting. Note the multifaceted, irregular surface on the stock bar (the white tape on this bar is simply a label).

3.2.3. Casting Process

The pieces were loaded into yttria crucibles in the proper proportions, with the higher-liquid-density component loaded on top of the other in an effort to induce mixing, rather than segregation, of the two. The crucibles were inserted into the MRF furnace, and the atmosphere of the hot zone was pumped down and then backfilled with argon: this was repeated three times in order to ensure as much as possible the purity of the argon atmosphere. After the third backfill, a slow flow of argon through the hot zone was established, and the melt was carried out according to a temperature program that ramped up to 1900°C in 60 minutes, held temperature for 20 minutes, then cooled back down to room temperature in 60 minutes. The actual maximum temperatures observed during this temperature program ranged between approximately 1850°C and 1880°C.

After having been removed from the crucible, the surfaces of the alloy slug were manually sanded in order to remove an interaction layer that developed between the alloy and the inside of the crucible. The samples were then melted a second time, in order to achieve a more homogeneous mixture of the component metals. The slug was inverted for the second melt, so that any segregation due to a density gradient from the first casting would be reversed. In addition, since the slug was to be re-melted anyway, additional source material was added at this point to increase the final yield of useful alloy. Following re-casting, which utilized the same temperature program, the interaction layer was once again removed. Further details of each individual casting, as well as images of the as-cast alloy slugs, can be found below in Table 4. This concluded the casting process, but one final step was necessary before diffusion discs could be cut from the as-cast alloy slugs: confirmation that sufficient homogeneity was achieved during the casting.

Table 4: Data pertaining to each casting of each alloy. Entries include the masses of elemental feed material used, expressed both in grams and as a percentage of the alloy, as well as the date on which each casting was performed.

Alloy:	U-50Zr	Zr-10Er	Zr-10Gd
First Cast	14.11g Zr (49.95%) 14.14g U (50.05%) June 12, 2012	18.99g Zr (90.00%) 2.11g Er (10.00%) July 12, 2012	20.68g Zr (89.99%) 2.30g Gd (10.01%) July 16, 2012
Second Cast	+8.74g Zr (49.95%) +8.76g U (50.05%) June 21, 2012	+10.33g Zr (89.99%) +1.15g Er (10.01%) July 25, 2012	+10.88g Zr (89.99%) +1.21g Gd (10.01%) July 20, 2012
Image	 44.59g	 32.29g	 34.52g

3.2.4. Post-Casting Homogeneity Analysis

Before diffusion discs could be cut from the as-cast slugs, it was necessary to ensure that a satisfactory degree of axial homogeneity in each slug was achieved during the casting process, so that all diffusion discs of a given alloy would all have the same composition. For this purpose, axial slices were cut from the edge of each of the alloy slugs and examined using EPMA. The burnable absorber alloys, which were analyzed first, can be seen below in Figure 12 as they appeared on the day of the analysis.

Figure 12: Axial slices of Zr-10Er and Zr-10Gd alloys prepared for EPMA examination.

Both qualitative (imaging) and quantitative examinations were carried out, and the results are as follows. In both alloys, some regions were seen to exist in a solid solution, while other regions existed in a two-phase structure of solute precipitates in an elemental zirconium matrix. While the entire sample would be expected to exist in the latter structure at this composition and ambient temperature, for both alloys, it is likely that in many places the solutes were still "frozen" in solution in a non-equilibrium structure due to the rapid cooling rate during casting (~30°C per minute), without sufficient time for precipitate nucleation to occur. Another possible explanation may be that in the regions exhibiting the solid solution structure, the concentration of solute was in fact still within the solubility limit; as will be seen in the following pages, solute concentrations were indeed often found to fall below the nominal 10wt%, and may have been low enough in places to be below the solubility limit. Phase diagrams for the Er-Zr and Gd-Zr systems can be seen below in Figure 13.

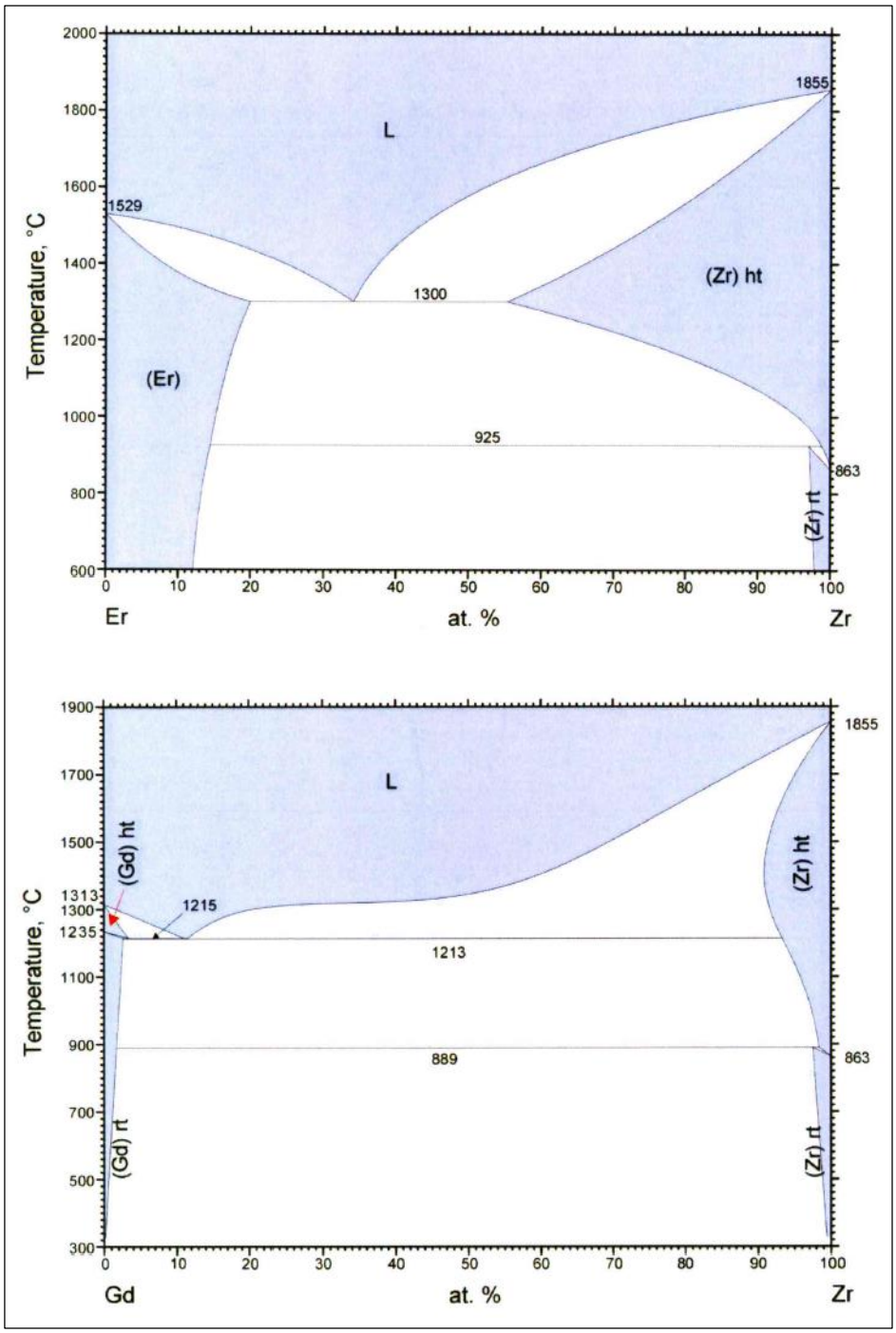

Figure 13: Phase diagrams for the Er-Zr and Gd-Zr systems. Graphics courtesy Lightbridge Corporation

A good example of the solid solution structure in the Zr-10Er alloy can be seen below in Figure 14. Figure 14(a) shows a backscatter electron (BSE) image of the region at a magnification of 200x, and Figure 14(b) shows an x-ray map of a small area within the region at 2000x. This x-ray map, created from the characteristic x-rays emitted from each element upon excitation from the electron beam, depicts zirconium in red and erbium in green.

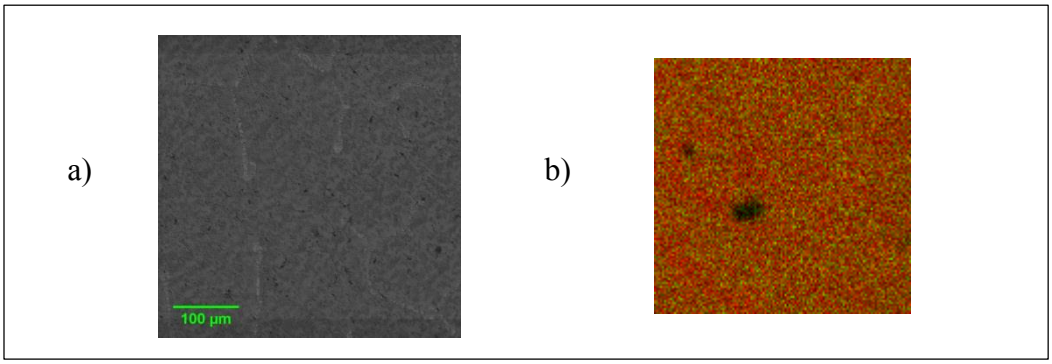

Figure 14: Example of solid solution phase structure.

Similarly, a good example of the two-phase structure can be found in the Zr-10Gd alloy, shown in Figure 15 below. The magnification levels are the same as above, with the x-ray map once again depicting zirconium in red and the solute in green, this time gadolinium.

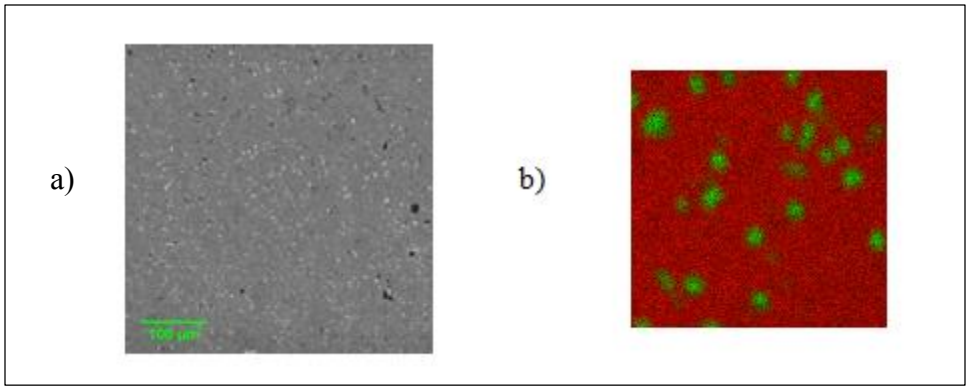

Figure 15: Example of two-phase structure.

In addition to these qualitative examinations, more rigorous quantitative measurement was carried out as well. For each alloy, measurements of the alloy composition were taken at each of three points within each of the ten selected regions, for a total of 30 composition spot-checks. These values were then plotted, as seen in Figure 16. Ideally, these plots would, of course, appear as a horizontal line at a composition of 10wt% solute.

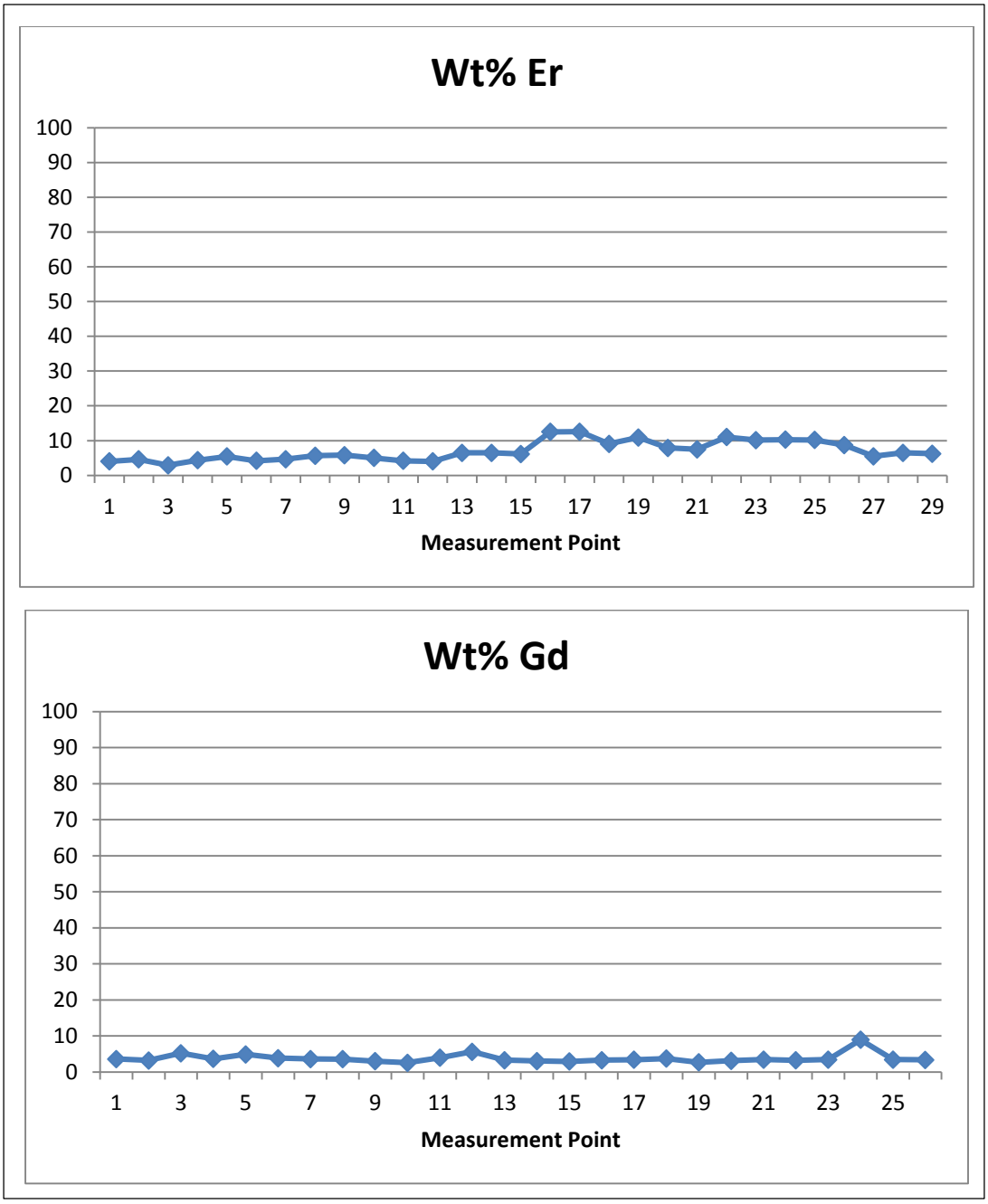

Figure 16: Measured alloy composition profiles over the axial height of the alloy slugs.

Both alloys generally exhibited a lower solute concentration than the nominal 10wt%. Recalling that the EPMA samples were sliced axially from the edge of the as-

cast slugs, this lanthanide depletion at the periphery of the slug was likely caused by interaction with the yttria crucible within which the casting was carried out. The composition was expected to adhere more closely to the nominal 10wt% of solute within the interior of the slug. For the purposes of this analysis, however, it should be recalled that the primary purpose of the axial examination was to ensure that there was not extensive axial segregation of the component elements, and it does indeed seem that such segregation was not the case. Both plots exhibit a reasonably flat composition profile. The Zr-10Er alloy did seem to have an elevated erbium concentration in the bottom half of the slug, as compared to the top half (measurement points are numbered top to bottom); however, it was decided that this degree of homogeneity was as high as could be reasonably expected, and that the cutting of diffusion discs would commence without further delay for additional melts. Indeed, the possibility always existed that additional melts could induce further segregation, rather than further homogenization.

Homogeneity analysis was then carried out for the U-50Zr alloy, although with some modifications to the techniques. The analysis was conducted in two steps: firstly, a rapid but less rigorous qualitative scan, followed by a (presumably) more accurate quantitative analysis (although, there were complications that may have caused some error in the quantitative analysis, as will be discussed shortly). The axial slices from the as-cast slug that were used in this analysis can be seen as they appeared just prior to analysis in Figure 17, having been mounted in epoxy, polished, and coated with a thin layer of conductive carbon to mitigate charge buildup on the surface.

Figure 17: U-50Zr axial sample prepared for EPMA examination.

The qualitative analysis consisted simply of a continuous scan over the entirety of both segments of the sample, recording raw count rates for characteristic X-rays from uranium, zirconium, oxygen, and yttrium. Yttrium was included in anticipation of contaminate inclusions in the alloy from the yttria crucible in which it was cast, and indeed such inclusions were found periodically. It should be emphasized that this data is of raw count rates only, and is not necessarily directly proportional to the relative abundance of the different components; it has not, for example, been in any way corrected for background counts rates or for the interference effects between the different elements present in the system. Consequently, there is no simple way to directly correlate these count rates to the alloy composition at a given point. However, this data does nevertheless provide a qualitative approximation of the composition profile throughout the sample. The plots shown in Figure 18 depict the raw count rates as collected by scanning the sample from the top of the slug to the bottom.

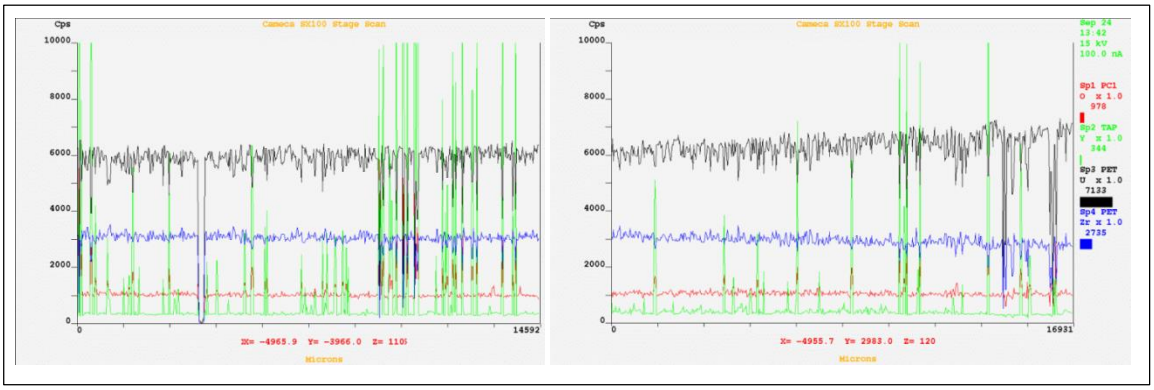

Figure 18: Plotted count rates measured from wavelength dispersive spectroscopy (WDS) in a continuous scan of the sample. Left to right, scan was carried out from the top of the slug to the bottom, in two segments. Colors are assigned as follows: uranium in black, zirconium in blue, oxygen in red, and yttrium in green.

While this data is, again, not very rigorous, useful conclusions could nevertheless be drawn from the above plots. The composition profile appeared quite uniform in the upper half of the slug, while the bottom half was shown to become progressively more uranium-rich farther down. This was to be expected, as the liquid uranium was more dense than the liquid zirconium during casting; however, the apparent degree of segregation was by no means excessive.

Next, quantitative analysis was carried out in order to attain more exact values for the elemental composition at a series of points in the sample. The measurements, however, were greatly complicated by the structural nature of the alloy, which consists of a uniform matrix with α-Zr precipitates, and consequently there may have been some error induced in the measured values. The measurement procedure utilized was as follows: in a given region, the compositions of the matrix and of the precipitates were measured, and the bulk composition in the region was then computed from the area

fraction of each phase in the region. There was, however, great difficulty in evaluating the area fraction of each of the two phases in a given region. As can be seen in the BSE images shown in Figure 19, there were not sharp boundaries between the α-Zr precipitates and the matrix; rather, the two phases share a very diffuse boundary. Furthermore, an additional complication is clearly portrayed in the high-contrast BSE image of the same region. The high-contrast version exposes the tendency for uranium-rich "halos" to form around the zirconium precipitates, regions in which there was localized zirconium depletion due to this component being pulled out of the matrix during the process of zirconium precipitate nucleation. This "halo" region was, therefore, yet another area with a different composition that is difficult to accurately account for in the aforementioned analytical procedure. Finally, the effects of contaminate yttrium inclusions must also be accounted for; however, this, at least, was relatively straightforward since the yttrium inclusions did exhibit sharp boundaries. In summary, there was a high degree of "grey area" (literally) in carrying out quantitative composition measurements of this alloy, and consequently there may be considerable error in the final values attained. These values, as measured at nine points distributed over the axial extent of the sample, are plotted in Figure 20, ordered from top to bottom as before.

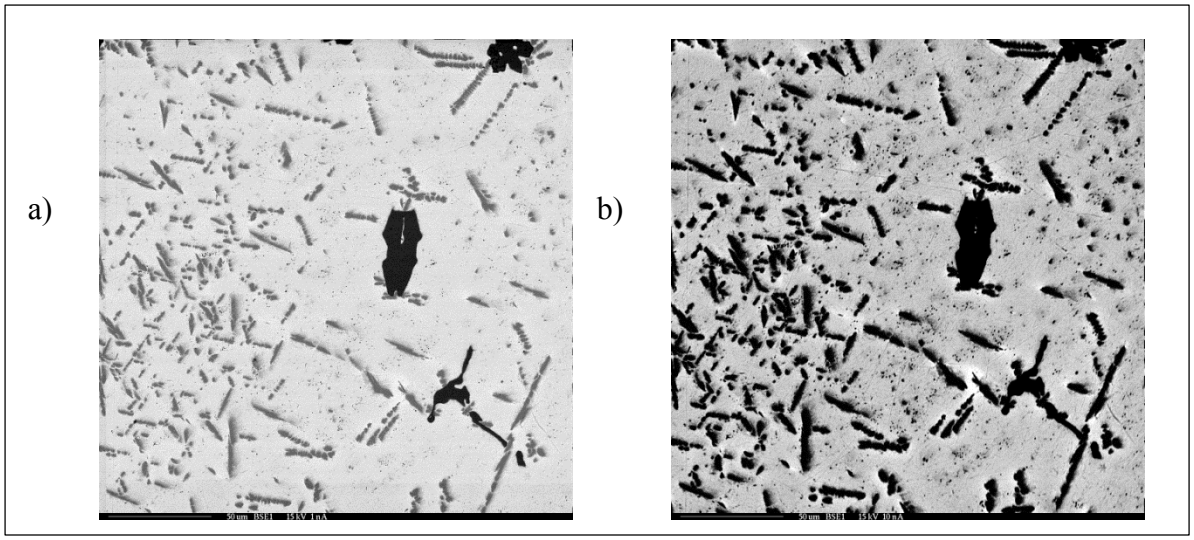

Figure 19: BSE images at 400x magnification of a region of the U-50Zr alloy with (a) standard contrast and (b) high contrast. Elements of higher atomic number appear brighter in BSE images; therefore, uranium is lightest in color, zirconium precipitates are grey, and yttrium inclusions are black. Note the brighter "halos" of localized zirconium depletion around the α-Zr precipitates.

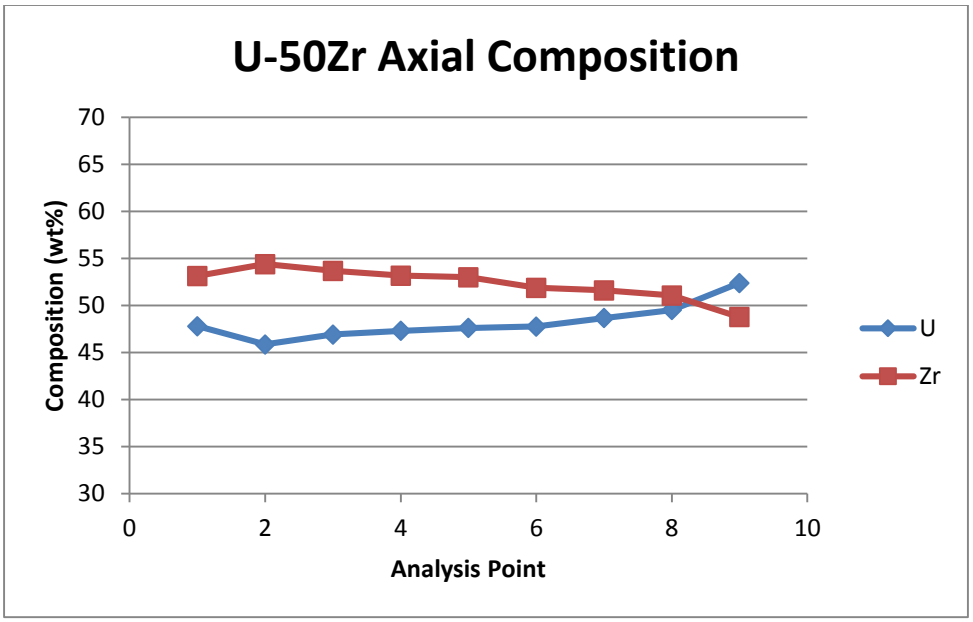

Figure 20: Measured alloy composition at a series of ten points descending down the axial extent of the slug.

While the above factors do reduce the reliability of the values found in Figure 20, the data does seem reasonable:

- The overall trends between the qualitative and quantitative analyses are in agreement.
- There is always an inverse relationship between the uranium and zirconium abundances, as would be expected; they never both increase or both decrease.
- Pairs of U/Zr composition values add up very close to 100% (within 1%) for all ten pairs.

Thus, it would seem that the data is reasonable. If the results can indeed be considered reliable, the findings were very positive: the alloy composition only deviated from the nominal 50/50 by a few weight percent in either direction. For an alloy created by melt casting with metals of different liquid density, this degree of homogeneity was quite satisfactory.

3.3. Preparation of Diffusion Samples and Furnace Apparatus

Having found all the alloys to be acceptably axially homogeneous, diffusion discs were cut from the as-cast slugs to be assembled in diffusion couples. In order to begin diffusion annealing, a clamping structure needed to be designed to hold the discs in contact together, and a furnace needed to be set up with all the necessary infrastructure to maintain the proper conditions during the annealing process.

3.3.1. Diffusion Couple Apparatus

The stack of diffusion discs was immobilized by a structure consisting of two flanges that were drawn together by three tie-rods. Stainless steel 410 was selected as the metal to be used for the tie-rods, as this material has a coefficient of thermal expansion within the proper range for this purpose. This same material was also selected for the nuts securing the tie rods, so as to not induce any differential thermal expansion between the two. Finally, the flanges were composed of stainless steel 304. Once some necessary modifications had been made to the stock parts in a machine shop, they were assembled together into the apparatus seen below in Figure 21.

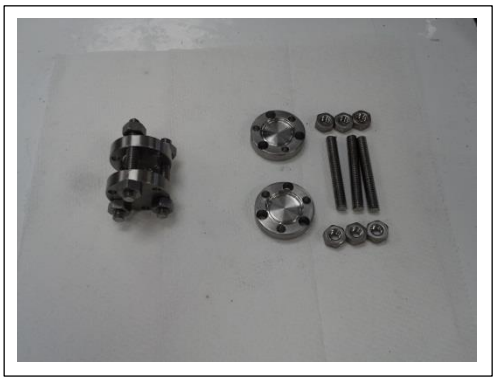

Figure 21: Structural apparatus for clamping diffusion discs together, shown fully assembled (left) and exploded view (right).

So as to prevent interaction between the clamping apparatus and the samples during diffusion annealing, inert foils were used as a barrier between these surfaces. Tantalum was selected as an appropriate material, and foils were stamped out from a sheet for this purpose.

Each sample disc was cut with a thickness of approximately 1.5 mm. The surfaces that were destined to become the diffusion interfaces were then polished down to a 6 μm (1200 grit) smoothness, as seen in Figure 22, in order to ensure proper contact between the surfaces during annealing. With the alloy discs thus prepared, they were inserted into an inert-atmosphere glovebox, together with the clamping apparatuses, to be assembled without oxidation of the polished surfaces.

Figure 22: A fine, mirror-like polish of the surfaces of U-50Zr diffusion discs.

At this juncture, it was necessary to consider the thermal expansion behavior of the diffusion couple components that would occur during the annealing. The degree of thermal expansion in the tie-rods needed to be low enough that the stack of sample discs would not become loose and fall out, but also needed to be high enough that the expansion of the sample discs would not induce so much stress that the tie rods could break. Thus, the degree of thermal expansion in the tie-rods needed to be smaller than

that of "the stack", but not by too great of a margin. The total thermal expansion of "the stack" is the manifestation of the combined expansion of each of the components: alloy samples, tantalum diffusion barriers, and stainless steel 304 end flanges. Initial calculations showed that the expansion of the stack would exceed that of the stainless steel 410 tie-rods by such a margin that the applied stress would well exceed the yield stress of the tie-rods. It was therefore clearly necessary to employ some device to reduce the thermal expansion of the stack relative to that of the tie-rods; this was achieved by including an elemental zirconium "buffer" in the stack with a thickness of 10 mm. Since the linear coefficient of thermal expansion (CTE) of zirconium is less than that of stainless steel 410, the inclusion of zirconium in the stack reduces the ratio of stack expansion to tie-rod expansion, thereby decreasing the amount of thermal stress induced during annealing, as shown in Figure 23 below. It was found that the addition of 10 mm of zirconium in the stack would reduce the thermal stress to an acceptable ~100 MPa. This value was found through calculations carried out using the Engineering Equation Solver (EES) software package; full details can be found in Appendix A. The inclusion of the zirconium buffer also had the added benefit that it could serve as an oxygen-getter, since elemental zirconium will oxidize readily at high temperature. All the pertinent values for the thermal expansion calculations are tabulated in Table 5 below, and the final diffusion couple assembly is depicted in Figure 24, as seen through the window of the glovebox in which it was assembled.

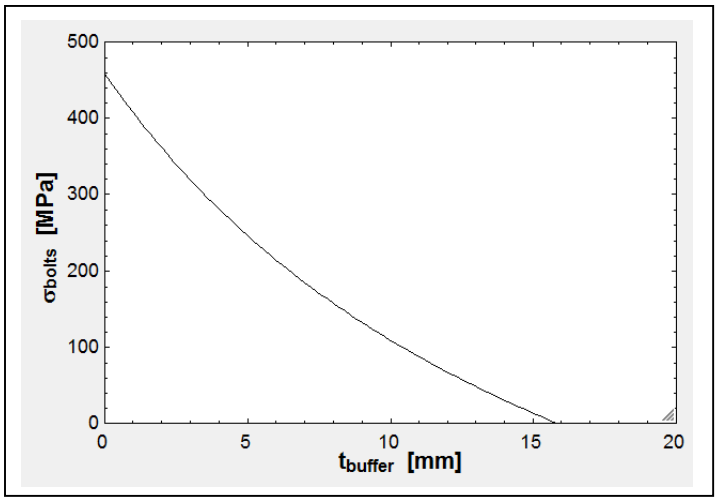

Figure 23: Plot demonstrating the relationship between the thickness of the zirconium buffer and the resulting stress in the tie-bolts.

Table 5: Approximate relevant material properties at 600°C.

Part	Material	CTE [µm/m-K]	E [GPa]	Yield Stress [MPa]	Thickness [mm]
Flanges	SS 304	18.7	193	290	6.5
Sample discs	Zr, basically	7.2	88	unknown	1.5 each
Ta foils	Ta	6.8	186	not needed*	0.2 each
Tie-bolts	SS 410	11.6	200	310	sum of above

*Tantalum yielding was not going to be a limiting factor in this structure

Figure 24: Diffusion couple, fully assembled except one tie-rod. Sample foils are visible on the right side, with the zirconium buffer on the left side, separated from the samples by a tantalum foil. Tantalum foils also separate the samples and the buffer from the stainless steel 304 flanges at either end. Note the white color of the tie-rods, which is due to a boron nitride lubricating coating.

3.3.2. Furnace Apparatus

Diffusion annealing was carried out within a Barnstead Thermolyne 21100 tube furnace coupled with a Eurotherm 2116 temperature controller. A series of measures were taken to ensure the steady, reliable, safe operation of the furnace throughout the annealing. First, an argon supply was assembled to slowly flow inert gas over the samples and thereby prevent oxidation at temperature. Shown in Figure 25, the argon supply system includes an oxygen trap, a moisture trap, two supply tanks in order to allow tank replacement without interruption, and a flow meter to control and monitor the volumetric flow rate through the system.

Figure 25: Argon supply, including oxygen and moisture traps.

A cooling system was also installed. The diffusion couples were contained within an aluminum oxide tube, and this tube protrudes somewhat from the top of the furnace, as can be seen in Figure 26. It was therefore necessary to ensure that this exposed segment of the alumina tube did not become too hot, for safety reasons as well as to protect the integrity of the rubber seals upon which the purity of the inert atmosphere relies. Therefore, a copper cooling jacket was placed around the alumina tube, through which water is circulated by a pump. The heat is then rejected to the air by a forced-convection radiator. Each of these components of the cooling system can be seen in Figure 26. Finally, an Omega HH306A datalogger recorded the temperature of the samples over time using a K-type thermocouple.

Figure 26: Furnace setup, including all cooling system components and datalogger.

The diffusion couples were loaded into the alumina tube within the glovebox, and the assembly was inserted into the furnace. The internal components of the alumina tube can be seen in Figure 27 below. A series of coils in the argon inlet line ensured the gas would be up to temperature when it reached the samples; heat shields at the top reduced heat transfer out of the system; and a K-type thermocouple measured the temperature near the bottom of the tube, where the samples were found.

Figure 27: Internal components of the alumina tube, including, left to right, the diffusion couples, thermocouple, argon pre-heating coils, and heat shields.

All preparations had now been made to commence diffusion annealing.

3.4. Diffusion Annealing

Diffusion annealing was commenced with an argon volumetric flow rate of <100 mL/min, and with measurements of the temperature recorded by the datalogger at 50-minute intervals. For a given annealing temperature, all samples to be annealed at that temperature were loaded in the alumina tube at the beginning, and removed one at a time as each completed its respective annealing duration. For example, for the 550°C samples, all three were loaded initially, and annealing was carried out for two weeks; at this point the two-week sample was removed, then annealed resumed for the other two samples for another two weeks; the four-week sample was then removed, and the last sample was annealed for another four weeks to reach the eight-week mark. In this way

all the annealing was completed in the minimum possible time. This did necessitate that the system be cooled to ambient temperature for samples to be removed; therefore, the four-week samples all experienced one cooling cycle, and the eight-week samples experienced two cooling cycles during their annealing. However, the additional time required to do every individual sample sequentially exceeded what was available for this study. All sample loading and unloading to and from the alumina tube was carried out under inert atmosphere in the glovebox. This therefore allowed no opportunity for oxygen to contaminate the system during sample exchange.

Following this scheme, Table 6 below summarizes the schedule for each of the annealing experiments carried out in this study.

Table 6: Annealing schedule for diffusion experiments.

Annealing Temperature	Time Elapsed	Date
550°C	Start	October 4, 2012
	2 weeks	October 18, 2012
	4 weeks	November 1, 2012
	8 weeks	November 29, 2012
600°C	Start	January 8, 2013
	2 weeks	January 22, 2013
	4 weeks	February 5, 2013
	8 weeks	March 5, 2013
650°C	Start	March 7, 2013
	2 weeks	March 21, 2013
	4 weeks	April 4, 2013

Temperature values were recorded by the datalogger throughout each diffusion experiment to provide a record of temperature fluctuations during the annealing. As can be seen below in Figure 28, the temperature controller performed well and did not allow hardly any temperature fluctuations to occur during the 600°C and 650°C runs (except, of course, those that were induced deliberately for sample removal at the two- and four-week intervals). Unfortunately, however, due to a problem with the datalogger during the first run, at 550°C, temperature data is unavailable for this anneal. It may also be observed in Figure 28 that the temperatures as measured by the datalogger did tend to be slightly above the nominal temperatures used for the setpoints on the furnace, respectively; however, the difference is small enough that each annealing still occurred within the intended phase region.

a)

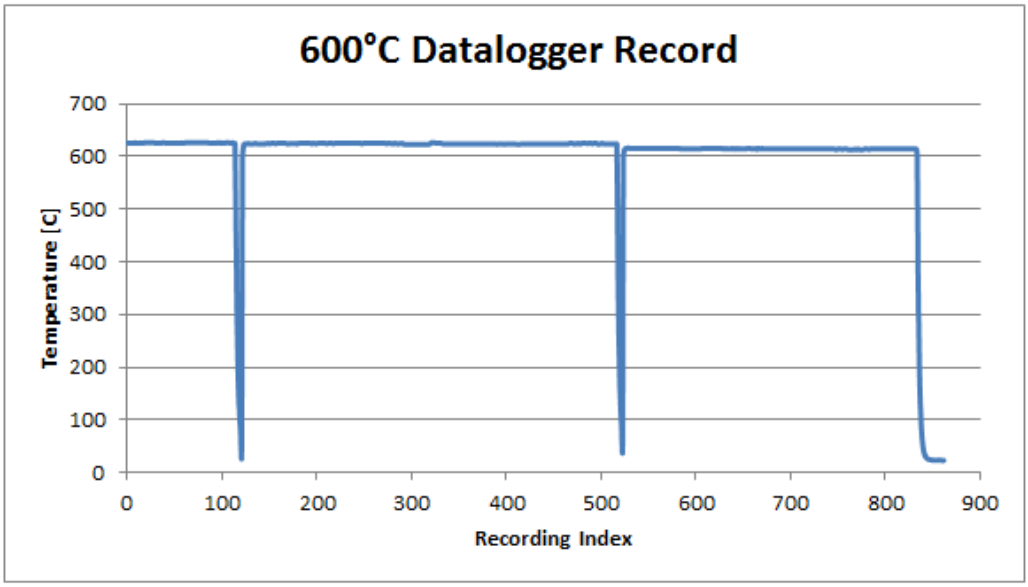

b)

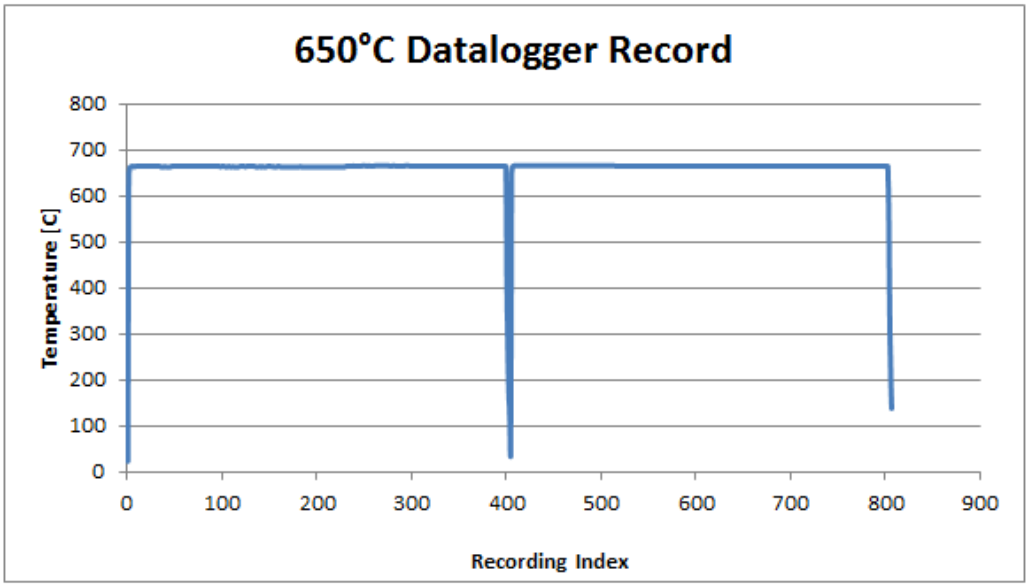

Figure 28: Datalogger temperature records for (a) 600°C anneal and (b) 650°C anneal.

3.5. Analytical Process

Upon completion of annealing, herein follows a discussion of the equipment, processes, and methods utilized in obtaining and analyzing the experimental data.

3.5.1. Electron Probe Microanalysis (EPMA)

In this work, elemental composition profiles across a diffusion interface were collected using an Electron Probe Microanalysis instrument; specifically, a Cameca SX50. This instrument bombards the sample with a beam of electrons that induce the emission of characteristic x-rays from target atoms. These x-rays are then detected by the system to determine elemental compositions using either energy dispersive spectroscopy (EDS) or wavelength dispersive spectroscopy (WDS). EDS is used to quickly provide a cursory indication of the general material composition, whereas WDS, capable of much better x-ray energy resolution, is used to carry out much more rigorous measurements of elemental abundances at the cost of much longer measurement times. The high energy resolution of WDS systems is made possible through the use of diffracting crystals and the application of Bragg's Law:

$$\boxed{n\lambda = 2d \sin\theta} \qquad \text{Equation 3}$$

where λ is the wavelength of the x-ray of interest, d is the spacing between atomic planes in the crystal lattice of a diffracting medium, θ is the angle between the incident photon and the atomic plane, and n is an integer. These parameters are illustrated in Figure 29.

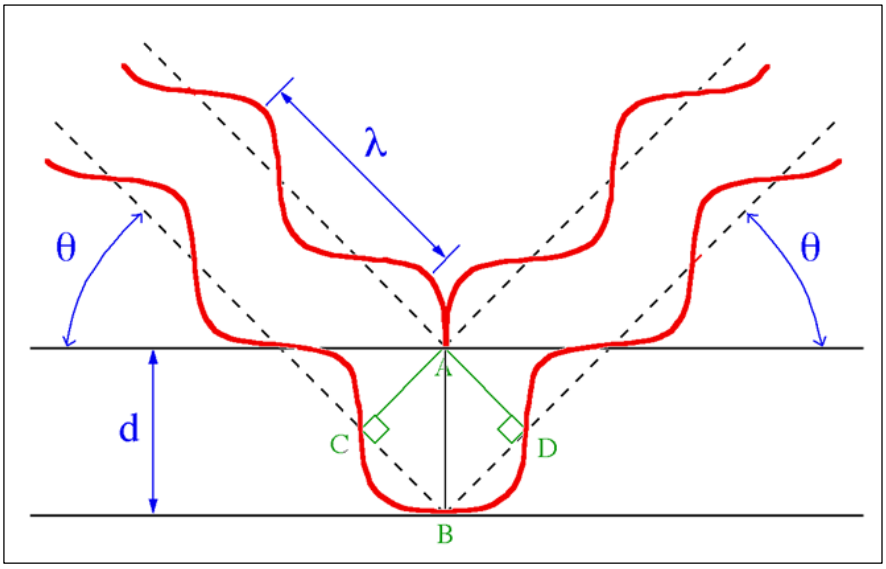

Figure 29: Schematic representation of the parameters related by Bragg's Law. Graphic courtesy Department of Geology, Texas A&M University.

These principles are applied in WDS systems to count only the x-rays that have a very specific wavelength. Using diffracting crystals with a known *d* value, the angle θ is modulated such that only x-rays of a select λ are efficiently diffracted in the direction of the detector, effectively filtering out x-rays of all other energies.

The EPMA instrument also allows imaging of the sample to be performed, most often through the detection of backscattered electrons (BSE), although secondary electron (SE) imaging is also used in some applications.

All of these features of the EPMA instrument are illustrated in Figure 30 below, as well as the components that focus and regulate the electron beam.

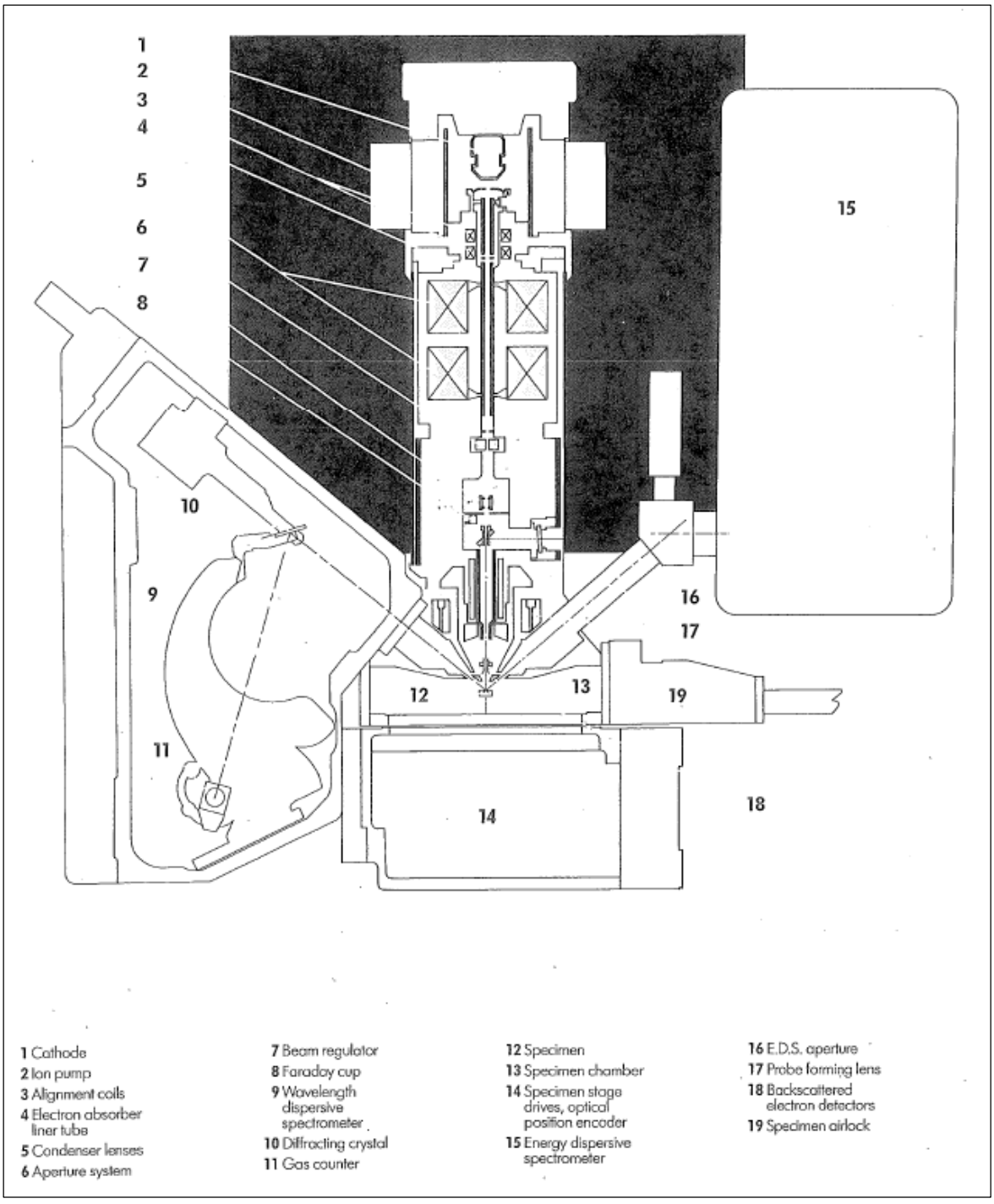

Figure 30: Cross-section of the EPMA instrument. Note the illustration of the WDS system (components 9, 10, and 11, on the left side of the diagram). Graphic courtesy Department of Geology, Texas A&M University.

Upon removal from the diffusion couple apparatus, samples were mounted in epoxy, sectioned, and the surface polished. A thin layer of conductive carbon was then deposited on the surface to mitigate charge buildup. A representative sample prepared for EPMA examination is shown in Figure 31. Then, the first step in analyzing the samples was to carry out optical scans of the sample surfaces. These scans, shown below in Figure 32, could then be imported into the sample navigator program and indexed to coordinates of the microprobe stage, allowing for easy sample navigation and selection of regions for analysis.

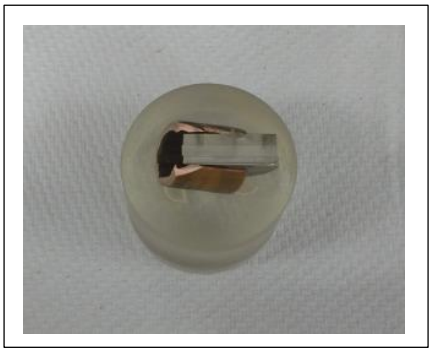

Figure 31: Representative diffusion sample prepared for EPMA analysis. The copper was put in place simply to stabilize the cluster of diffusion discs during epoxy mounting.

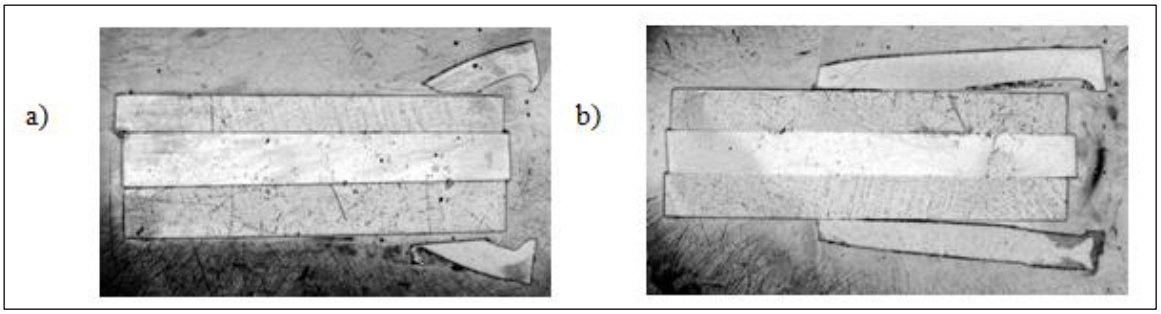

Figure 32: Scans of representative samples, used in the sample navigator program.

Having completed this indexing, the samples were then viewed through BSE imaging, in order to identify different grains and phases within the samples. Since BSE imaging is highly Z-dependent, this technique can be used to easily distinguish between regions of differing composition. Such imaging quickly revealed the systems to be very complex, for the following reasons. All three alloys under study exhibited very heterogeneous structures consisting of precipitates of one phase embedded in a matrix of another phase. The abrupt change in composition between the matrix and precipitates would, of course, complicate attempts to measure concentration profiles with WDS line scans. In addition, yttria inclusions were found, artifacts from the casting process used to initially fabricate the alloys. Furthermore, a large proportion of the distance along each of the interfaces lacked sufficiently intimate contact between the alloys to be useful for WDS data collection; large gaps between the materials would, once again, compromise the collection of suitable concentration profiles. All of these factors needed to be considered in selecting appropriate regions for quantitative analysis. Figure 33 below provides a comparison between a relatively "clean" diffusion interface and another that is much less suitable for WDS measurements.

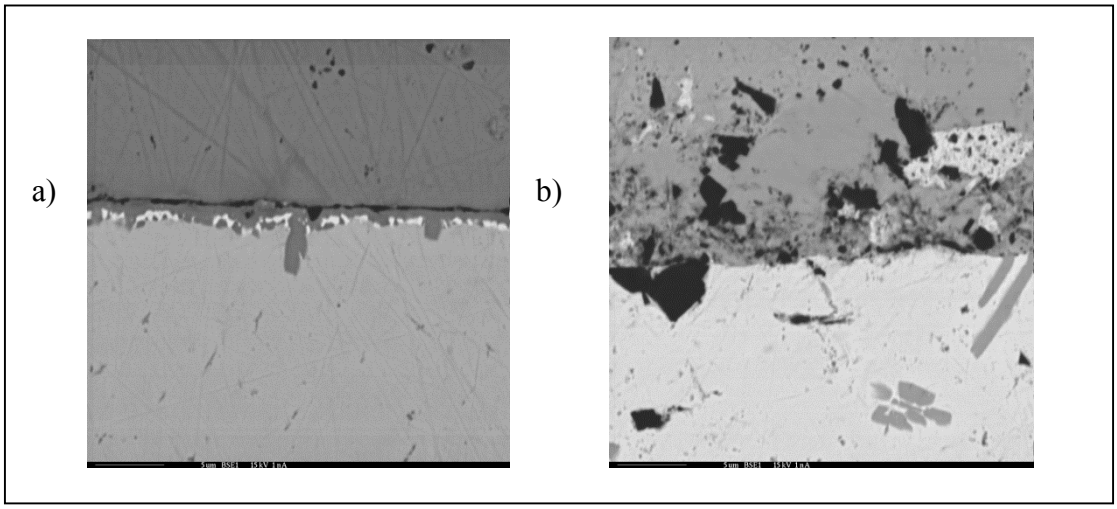

Figure 33: Illustrative example of (a) a satisfactorily "clean" region and (b) a much more complex region along material interfaces, both depicted through BSE imaging at a magnification of 3000x.

The next step in preparing for WDS analysis involved the selection of the analytical conditions. This includes, most notably, the accelerating voltage, current, and size of the electron beam; also, for each element to be analyzed, the x-ray line, diffracting crystal, background interval, and crystal operation mode (integral or differential) needed to be selected. Finally, inter-element interferences had to be considered to ensure adequate statistics could be attained for each of the x-ray lines of interest.

For the relatively heavy elements analyzed in this study, it was determined that the Lα line would be suitable for most of the elements of interest, namely, zirconium, erbium, gadolinium, yttrium, and hafnium. The Mα line would be used for measuring uranium. The accelerating voltage then needed to be selected such that, optimally, it

would exceed the critical excitation energy of the x-ray line by approximately a factor of 1.5 for each element. The value selected was 15 kV.

Counts were then taken from standards to find the appropriate beam current such that count rates would be high enough to attain good statistics, but not so high that detector dead time would have adverse effects. This value was found to be 100 nA of current in the electron beam, with a beam size of 1 micron. These conditions would yield high-resolution measurements of concentration profiles without causing significant thermal damage to the samples.

Finally, interferences between the x-rays of different elements needed to be considered in order to select which crystals would be used for which elements, and under what operational conditions. In order to count a given characteristic x-ray accurately and efficiently, the "sine theta" position of a diffracting crystal for the x-ray should not be at either of the extreme limits of the crystal's detecting range, nor should there be other high-intensity x-rays nearby. Differential mode was necessary if there were nearby higher-order interferences for a given x-ray; otherwise, integral mode was used. Background intervals were selected in order to fully span the width of the peak of interest. Also, crystals were allocated so as to divide up counting time, in order to complete counts with the smallest amount of total time. Finally, a suitable standard was selected for calibration peak-searches for each x-ray of interest. Considering all of these parameters collectively, selections were made for the WDS analytical conditions, and these conditions are summarized in Table 7 below.

Table 7: Analytical conditions for WDS examination.

Element	X-ray	Spectrometer	Crystal	Mode	Background Interval	Standard
U	Mα	3	PET	Differential	±700	$7UO_2$
Zr	Lα	3	PET	Differential	±700	6Zr
Er	Lα	4	LIF	Integral	±500	$6ErPO_4$
Gd	Lα	4	LIF	Integral	±500	$6GdPO_4$
Hf	Lα	4	LIF	Integral	+1100, -550	7Hf
Y	Lα	3	PET	Differential	±700	$6Y_2O_3$

With all of the analytical conditions specified, the next step in preparation for quantitative WDS analysis was to perform spectrometer verification for each x-ray of interest. In this calibration procedure, peak positions are measured and reconciled with their respective theoretical positions. Since peaks can shift due to temperature fluctuations, aging of the detectors, valence electron and chemical bonding configurations, etc., this is an essential step before quantitative analysis to ensure the quality of the measured data.

Finally, the analytical macro was specified. Based on the previous examinations, suitable regions for analysis were chosen in the samples. Coordinates for line scans were input into the macro, as well as appropriate counting times based on the x-ray intensities and expected concentrations of each element, respectively. Once all of this information was specified in the macro, quantitative WDS line scans were initiated. The composition data was then plotted to attain composition profiles across the interface for

each element of interest. Information pertaining to each of the individual analyses carried out in this study can be found in Table 8 below.

Table 8: Summary of EPMA diffusion analyses carried out in this work.

Analysis Date	Samples
November 6, 2012	Standard and 2wk550
December 12, 2012	4wk550 and 8wk550
February 13, 2013	2wk550 and 2wk 600
March 20, 2013	4wk600 and 8wk600
April 10, 2013	2wk650 and 4wk650

3.5.2. The "Standard" Sample

In addition to the diffusion samples, a "standard" sample was prepared and analyzed for comparative purposes. The standard sample was composed of discs of the same alloys as in the diffusion couples, but in an unreacted state, without having undergone diffusion annealing. Such a standard was deemed necessary in order to compensate for the phenomenon of x-ray fluorescence in EPMA analysis at a boundary between materials, which is represented schematically in Figure 34 below. In this phenomenon, the electron beam, incident on component A, induces a characteristic x-ray to be emitted, which then crosses the boundary into component B. This x-ray in turn causes a subsequent ionization event that results in the emission of a characteristic x-ray from component B. This second characteristic x-ray is then detected by the system. In this way, atoms from component B appear to be present in component A, since x-rays from component B are being detected while the electron beam is incident on component

A. This resembles diffusion in appearance, and causes artificially high computation of diffusion rates (Goldstein, et al., 2003). Thus, in diffusion studies this effect must be quantified using a sample that has not been annealed, then subtracted out from the data gathered from annealed samples. As it turned out, however, the effects of x-ray fluorescence in this system were too small to resolve from background noise, so no modification was made to the experimental data in compensation for this effect.

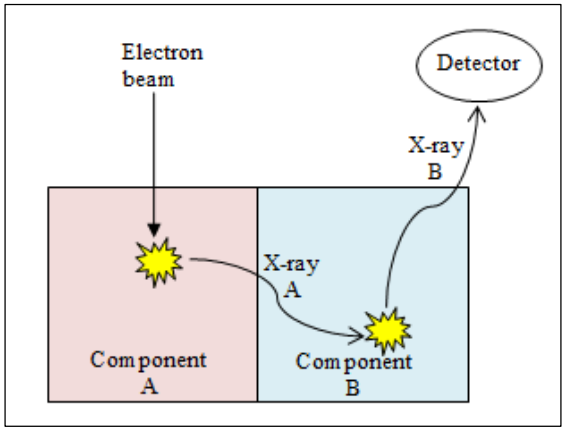

Figure 34: Schematic representation of x-ray fluorescence.

3.5.3. Computation of the Diffusion Coefficient

Once composition profiles had been acquired, the value of the diffusion coefficient could be calculated for each component in the system. As discussed in Section 2.2, there was some ambiguity as to the expected structure of the diffusion interface: whether it would appear as a two-phase precipitate region, or as a series of layered intermetallic compounds. In fact, when diffusion profiles were collected, it

became evident that both structures formed, the former structure developing in the δ-phase system, as observed by Akabori, et al, and the latter structure developing in the γ-phase system, in agreement with the Gibbs Phase Rule. This distinction is illustrated in Figure 34 below.

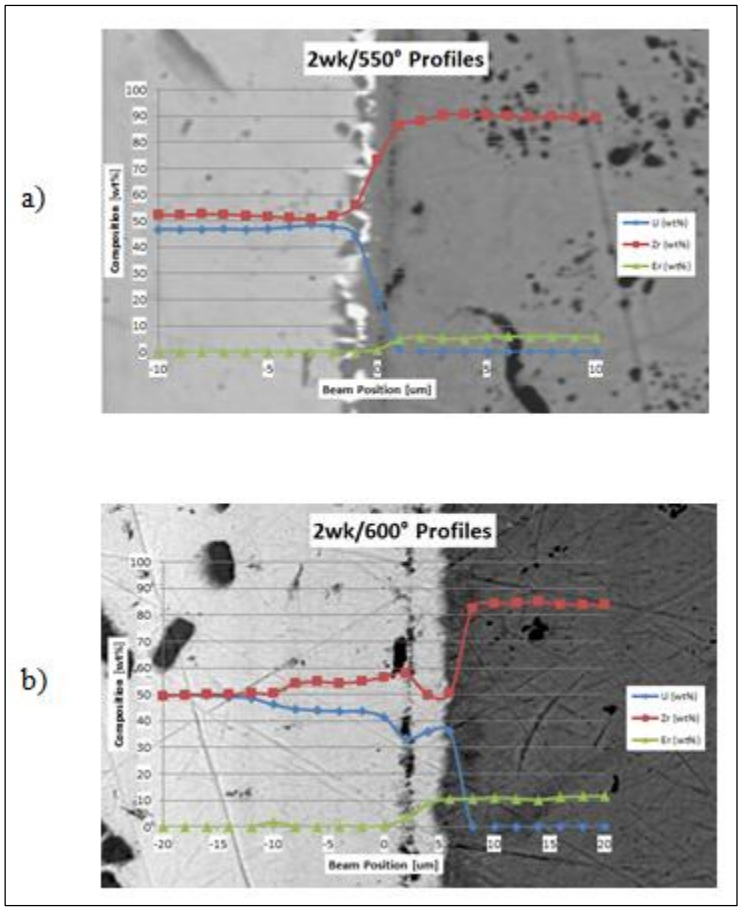

Figure 35: Comparison of diffusion profile characteristics in (a) the δ-phase and (b) the γ-phase, both in the U-50Zr/Zr-10Er system. Composition profiles are superimposed on the BSE image of the area analyzed, at a 1:1 scale. Note the distinctions in the features of the composition profiles and the interaction zone structures.

The diffusion coefficient can be quantified from experimentally-obtained composition profiles using the following equation proposed by Wagner (Wagner, February 1969), under the assumption that composition change within a given individual phase is negligible:

$$D_i = \frac{(N_i - N_{i-1})(N_{i+1} - N_i)}{(N_i'' - N_i')(N_{i-1}'' - N_{i+1}')} K_{II} \qquad K_{II} = \frac{\Delta x^2}{2t}$$ Equation 4

where D_i is the diffusion coefficient for component *i*, K_{II} is termed the *intrinsic growth constant*, *x* is the diffusion distance, *t* is the time in seconds, and all composition parameters are as represented graphically in Figure 36, below. This method is known as the Wagner/Li-Powell method (Wagner, February 1969) (Li & Powell, 1985).

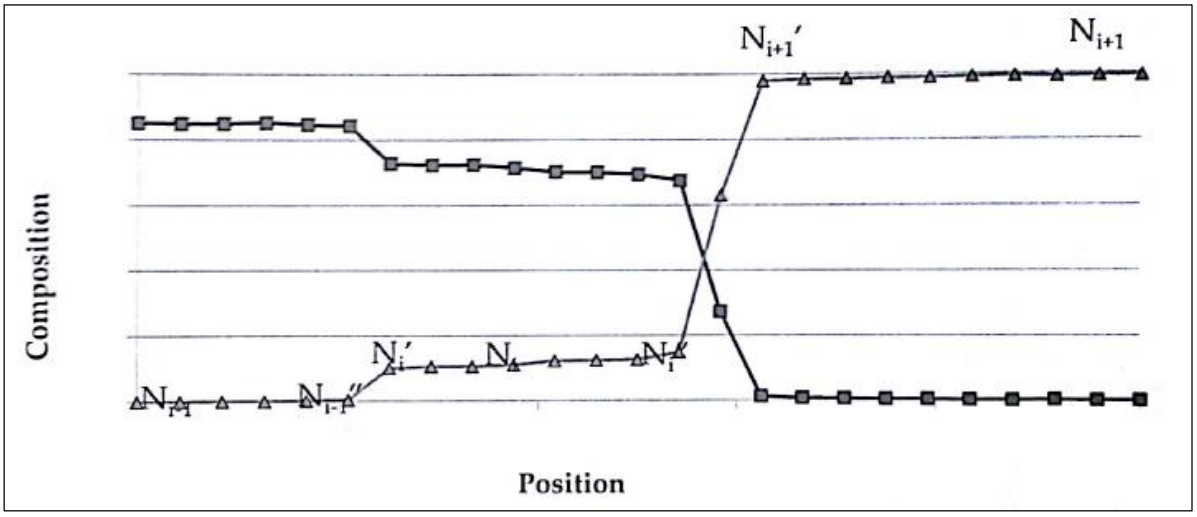

Figure 36: Graphical representation of composition parameters utilized in the application of Equation 4 for the computation of the diffusion coefficient for an arbitrary set of composition profiles. Graphic courtesy Grant Helmreich.

It is appropriate at this stage to interject a caveat with regard to some measures that were taken in processing the experimental data for these calculations. Diffusion experiments in an ideal world would yield concentration profiles that monotonically increase or decrease across a diffusion interface; experimental work in the real world, however, is far less obliging, and consequently complications invariably arise. As has been discussed previously, the materials related to this study exhibit highly heterogeneous structures, featuring precipitates and inclusions in which elemental compositions vary widely. Some of these are artifacts of the casting process; some are intrinsic to the alloys themselves. As a result, certain measures were necessary to condition the data for analysis.

Sudden, sharp compositional variations were present in the experimental data if the WDS line scan encountered a precipitate or inclusion in the material structure. Such compositional variations, however, are of course not the effect of diffusion phenomena, and in such cases various techniques were employed to remove these interferences from the data. In some cases, the "tails" of the diffusion profiles were truncated before the heterogeneity was reached; in other cases, linear interpolation was used to mitigate the effects of heterogeneities. An example of such data conditioning is illustrated below in Figure 37.

Such measures do, of course, have an impact on the integrity of the data; however, every effort was taken to apply these measures as consistently and objectively as possible, in order to maintain the integrity of the data as much as possible. While it is

perhaps regrettable that these modifications were necessary, such is often the case in experimental work, especially when such highly heterogeneous materials are involved.

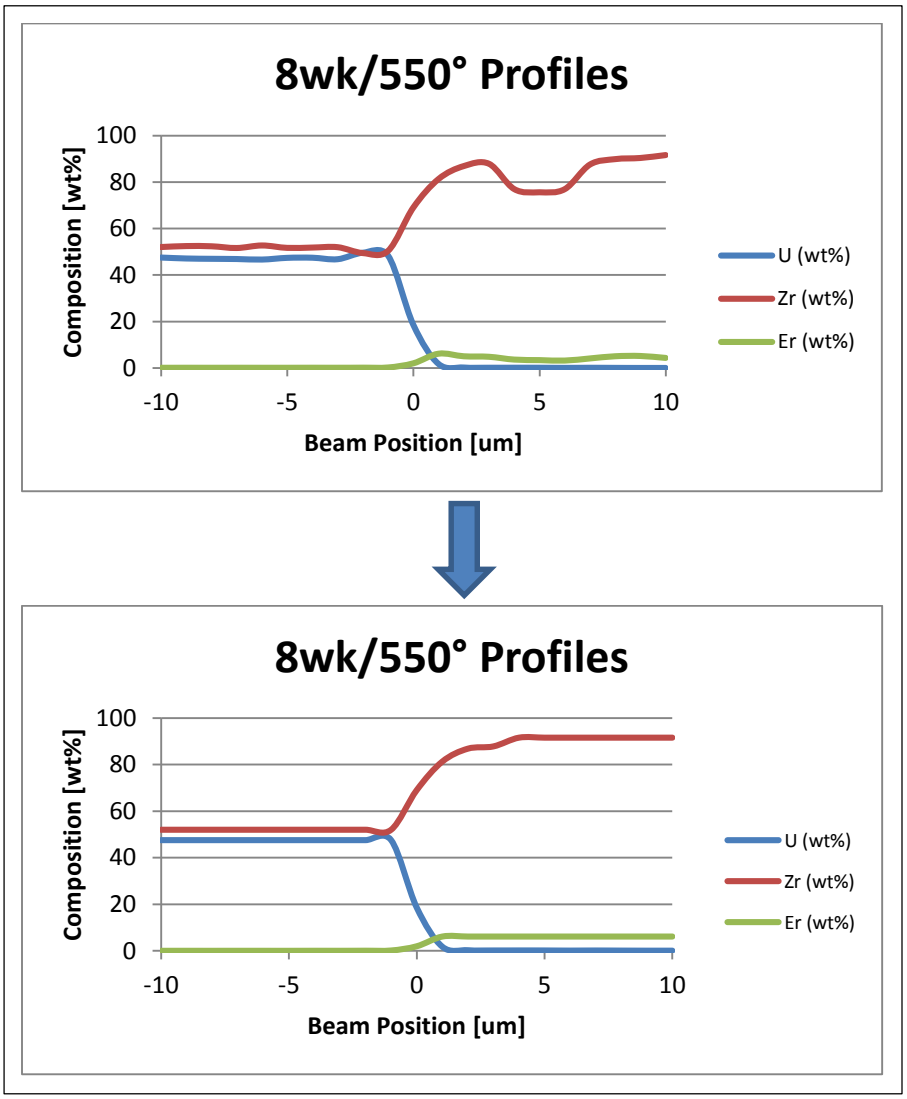

Figure 37: Example of the application of smoothing methods to mitigate the effects of heterogeneities in analyzing diffusion profile data. Note the removal of the inclusion that was encountered in the zirconium profile.

3.5.4. Oxygen Analysis

Qualitative analysis of contaminate oxygen concentration was also performed in this study. Rigorous quantification of precise oxygen concentrations, however, could not be attained in this work due to the limitations of the EPMA instrument for light element analysis. The very low-energy characteristic x-rays that are emitted from light elements are very difficult to count accurately: they suffer high loss to absorption along the path from their generation in the sample to their detection by the system, and even if they reach the detector, the gas-flow proportional counters used in the WDS system have very low detector efficiency at these x-ray energies. In addition, the energy spectrum of natural background x-ray radiation includes a peak in the low-energy region, resulting in a poor peak-to-background ratio when attempting to count low-energy x-rays. Similarly, it is also more difficult to distinguish low-energy signals from the electronic noise in the detection system. Furthermore, the degree of oxidation that occurs on the surface of a sample is often much more extensive than that within the bulk of the material, and consequently measured values of the oxygen concentration are grossly overrepresented by the effects of the surface layer. Finally, the detection of low-energy x-rays becomes even more challenging in systems with heavy elements present (such as uranium, erbium, and gadolinium); the very complex electron clouds around these heavy elements allow for a very large number of possible electron transitions, each with its own respective energy change, and the probability is very high that there will be strong interferences with the low-energy x-ray of interest. All of these factors limit the ability

of the EPMA instrument to produce accurate, reliable data for light element concentrations.

Therefore, WDS measurements were not utilized in this study to produce plots of the oxygen concentration at the diffusion interfaces of the samples. Rather, these plots were generated qualitatively by collecting x-ray maps, as seen in Figure 38(a) below, and using image processing software to plot the average pixel value per column. Pixel values range from 0 to 255, with 0 being pure white and 255 being pure black. Since brighter areas correspond to higher oxygen x-ray counts, the image was inverted, as seen in Figure 38(b), and then the plot of average pixel value was generated, so that higher plot values correspond to higher oxygen content. This therefore provides a qualitative representation of the general oxygen distribution, but cannot be directly associated with exact values for the oxygen concentration. All of the oxygen concentration plots generated in this study can be found in Appendix C.

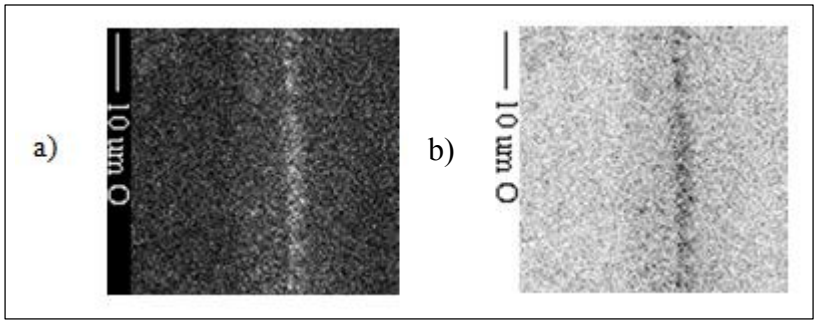

Figure 38: Representative x-ray map (from the 2wk600 sample) at 2000x magnification used in generating oxygen profiles, (a) before inversion and (b) after inversion.

4. RESULTS

With two exceptions, experimental diffusion profiles were collected and values of the diffusion coefficient computed for each sample included in this study. The exceptions were the 8wk600 and 4wk650 samples; when these specimens were examined under EPMA, it was found that the diffusion interfaces had separated, and that gaps of approximately 20-40 μm had developed between the alloy discs, as can be seen below in Figure 39. This therefore precluded the collection of any meaningful data from these samples.

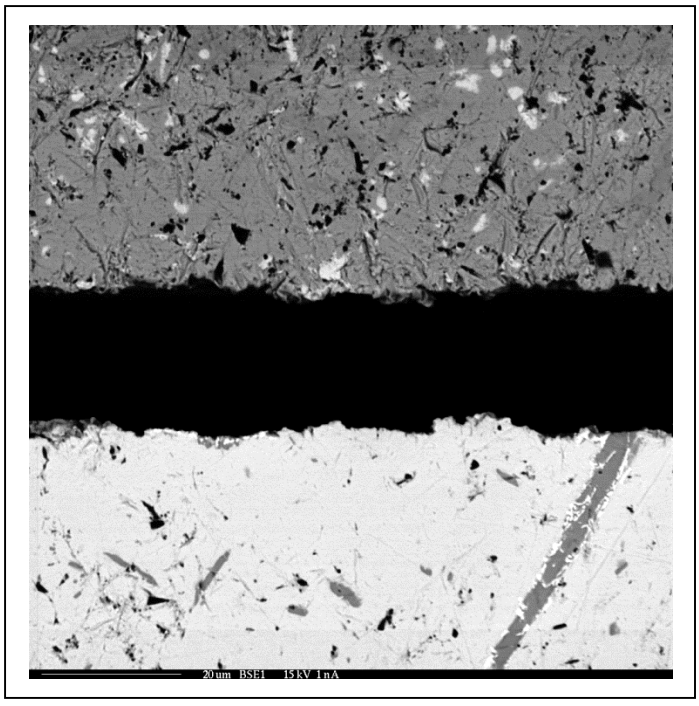

Figure 39: BSE image of the 4wk650 sample showing a gap of approximately 20 μm having developed between the alloy discs.

It is suspected that this separation was caused by rapidly quenching the samples upon completion of diffusion annealing. Since the annealings for the 8wk600 sample and 4wk650 sample were carried out in the δ+γ phase region and γ-phase region, respectively, as shown in Figure 2 (page 3), it was conjectured that upon cooling into the δ-phase region at the conclusion of the annealing the phase transformation could affect the diffusion interfaces and subsequently induce error in the calculation of the diffusion coefficients. Rapid quenching was proposed as a way of preserving the higher-temperature structure, as it would not allow sufficient time for appreciable restructuring. All of this would, of course, have applied to the 2wk600 and 4wk600 samples as well; however, annealing of these two samples had already been completed when the idea of quenching was first considered. It is believed that the separation of the diffusion discs was caused by the alloys contracting as they were rapidly cooled, rendering these samples useless. Quenching of the 2wk650 sample was successful, however, having caused no observable ill effects on the diffusion interfaces.

4.1. Diffusion Coefficients

Analysis was successful on each of the other six samples, however. All of the diffusion profiles that were collected in this study can be found in Appendix B, and the values of the diffusion coefficients calculated from these profiles, for each species in each system, can be found below in Table 9. These values represent the average of the individual diffusion coefficient values calculated at each of the different annealing times. Since the diffusion coefficient should be the same regardless of the annealing time, the

values of the diffusion coefficient were averaged across the temporal data points to yield the values presented below.

Table 9: Values of the diffusion coefficient obtained in this study.

U-50Zr/Zr-10Er System			U-50Zr/Zr-10Gd System		
Temperature [C]	Species	D [m^2/s]	Temperature [C]	Species	D [m^2/s]
550	U	$6.523\pm0.457 \times 10^{-20}$	550	U	$1.001\pm0.0701 \times 10^{-19}$
	Zr	$9.186\pm0.643 \times 10^{-20}$		Zr	$1.175\pm0.0823 \times 10^{-19}$
	Er	$4.657\pm0.326 \times 10^{-20}$		Gd	$1.242\pm0.0869 \times 10^{-19}$
Temperature [C]	Species	D [m^2/s]	Temperature [C]	Species	D [m^2/s]
600	U	$2.970\pm0.208 \times 10^{-17}$	600	U	$7.226\pm0.506 \times 10^{-17}$
	Zr	$2.819\pm0.197 \times 10^{-17}$		Zr	$7.501\pm0.525 \times 10^{-17}$
	Er	$1.393\pm0.0975 \times 10^{-17}$		Gd	$5.327\pm0.373 \times 10^{-18}$
Temperature [C]	Species	D [m^2/s]	Temperature [C]	Species	D [m^2/s]
650	U	$1.062\pm0.0743 \times 10^{-16}$	650	U	$9.175\pm0.642 \times 10^{-17}$
	Zr	$3.702\pm0.259 \times 10^{-17}$		Zr	$9.644\pm0.675 \times 10^{-17}$
	Er	$5.301\pm0.371 \times 10^{-17}$		Gd	$1.148\pm0.0804 \times 10^{-17}$

This data is also depicted graphically in the Arrhenius plot found below in Figure 40. This plot includes all of the diffusion coefficient data from this study, as well as that from the studies carried out by Akabori, et al and Rothman (Rothman, May 1961). This therefore allows all of these sets of data to be compared with one another, inclusively.

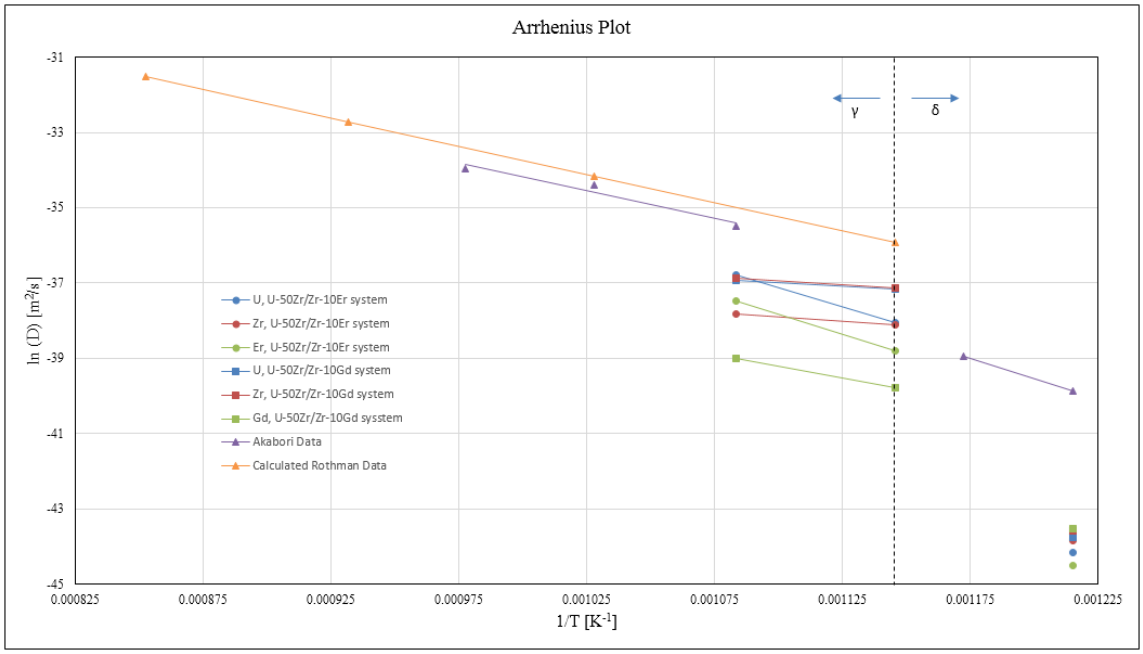

Figure 40: Arrhenius plot of diffusion coefficient values. Data sets from the U-50Zr / Zr-10Er system are shown using a circular marker; those from the U-50Zr / Zr-10Gd system are shown using a square marker; and those from external studies are shown using a triangular marker.

4.2. Causes for Error

As with any experimental work, this study has, of course, been subject to some possible causes for error. Some of these have been mentioned previously, but are discussed more fully here. While this is not a comprehensive listing of every conceivable cause for error, the following are some of the most noteworthy examples.

Firstly, recalling Figure 33 (page 51), it is clear that many of the diffusion interfaces exhibited very heterogeneous structures, featuring various precipitates and inclusions in which the elemental compositions varied widely. Recalling Figure 19 (page 33), these features also very likely caused modifications to the matrix composition

in the near vicinity. As a result, elemental compositions in these alloy systems were subject to considerable local variation, and therefore measurements carried out at arbitrary locations could potentially exhibit considerable variation as well. Careful and consistent selection of measurement locations may have helped to mitigate these factors; nevertheless, severe heterogeneities in the material structures may have been a significant cause of error in this study.

Additionally, as discussed previously at the end of Section 3.5.3, the experimental data underwent some conditioning in an attempt to mitigate the effects of these heterogeneities that were manifested in the composition profiles. While these measures were, of course, undertaken in an effort to make the data *more* representative of the actual diffusion profile, rather than less so, it must be recognized that such modifications must induce some additional uncertainty.

Error may have been introduced as well simply by the physical nature of the atoms under examination in this study. Rare earth elements, and indeed all heavy elements in general, can be difficult to analyze using WDS due to their very large electron clouds. With such a complexity of electron orbitals, there is an extremely large number of possible electronic transitions. Specifically, the number of possible transitions in an electron cloud of n orbitals is equal to $\frac{1}{2}*(n^2-n)$; of course, there are not nearly as many orbitals as there are electrons, since multiple electrons will occupy a given orbital, but nevertheless the uranium atom, as an example, includes 92 electrons distributed into 18 orbitals, for a total of 153 potential electron transitions, and as many

x-ray emission lines. Figure 41 below illustrates all of the possible electron transitions in an arbitrary (and very heavy) atom.

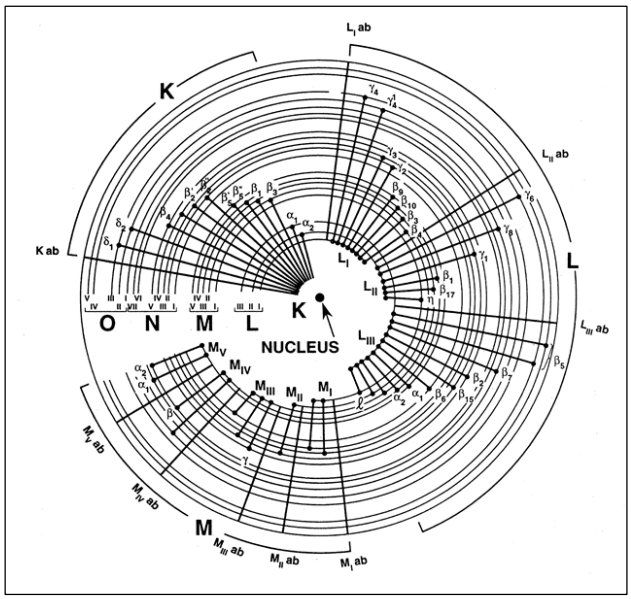

Figure 41: Schematic representation of all the possible electron transitions in an arbitrary heavy atom. Image adopted from (Goldstein, et al., 2003).

Most of these transitions are in fact extremely unlikely, but nevertheless heavy elements produce very complicated x-ray emission spectra. Inter-element interferences therefore become a major concern in WDS measurements when multiple heavy elements are present in the system, and these complicated spectra overlay one another. Interferences were, of course, taken into account in the WDS measurements performed in this study, but the corrections applied by the WDS system can be increasingly erroneous with increasing atomic number. With the presence in this study of uranium,

erbium, and gadolinium, all very high-Z elements, x-ray interferences may have been a considerable cause for error in WDS concentration measurements.

Finally, the presence of oxygen contamination in the samples may have caused the calculated values of the diffusion coefficient to be artificially low. Metal oxides in general are very stable structures, and their formation at the diffusion interfaces would have reduced atomic mobility and inhibited diffusion. As can be seen in the qualitative oxygen profiles found in Appendix C, it does indeed appear that in general oxygen concentrations were elevated at the interface, and oxide inclusions were observed in some of the x-ray maps collected under EPMA examination. An example of such an x-ray map exhibiting oxide structures is shown below in Figure 42. It can also be observed by comparing the x-ray maps and BSE images shown below in Figure 43 that in general oxygen was most highly concentrated at the original interface, but less so in the diffusion zone.

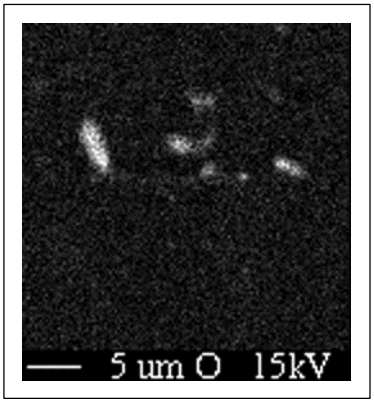

Figure 42: Representative x-ray map at 3000x magnification revealing a scattering of oxide grains (the bright grains) near the diffusion interface. This region was observed in the U-50Zr/Zr-10Gd system in the 4wk600 sample.

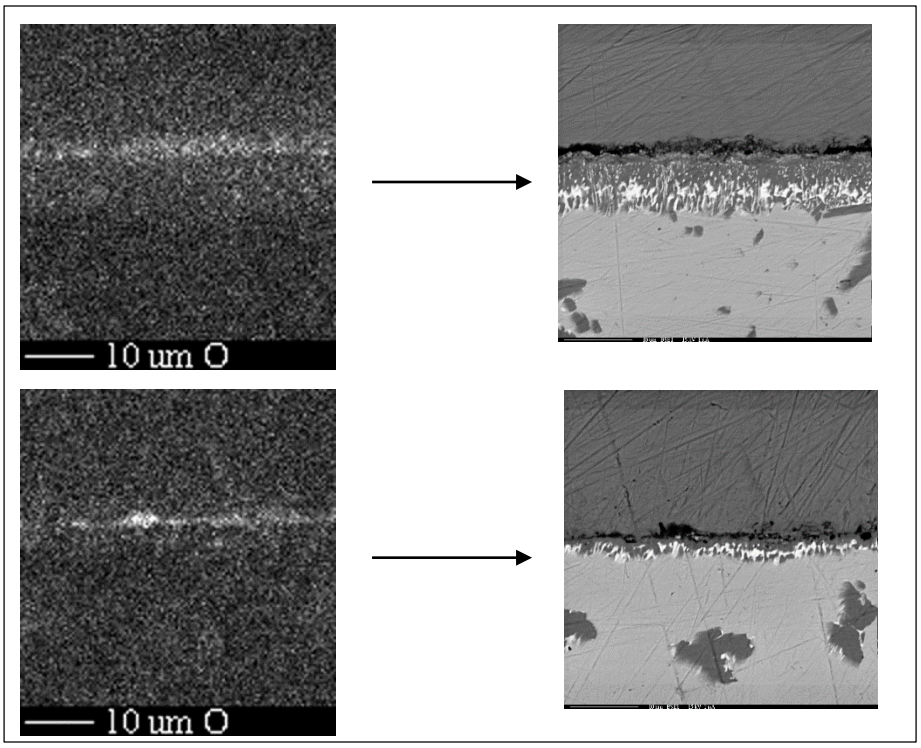

Figure 43: Comparison of oxygen x-ray maps and BSE images, demonstrating that oxygen was most highly concentrated at the original interface between alloys, but only slightly above the bulk concentration in the diffusion zone.

Such regions with oxide formation were easily identified from the x-ray maps, and therefore avoided for quantitative WDS analysis; nevertheless, a certain level of oxygen contamination was ubiquitous, and such contamination may have considerably reduced diffusion rates, thereby resulting in artificially low values of the calculated diffusion coefficient.

These are some of the more notable possible causes of error in this work. While this is certainly not a complete listing, the above factors probably made the most significant contributions to the experimental error in this study.

4.3. Statistical Uncertainties

For WDS measurements of elemental concentrations carried out in a typical EPMA system, including those carried out in this study, an accuracy of about ±1-2% of the amount present for a given element can be expected (Goldstein, et al., 2003). This uncertainty value can be greater for analyses of minor elements, those present at concentrations of less than about 10wt%, as is the case for erbium and gadolinium measurements in this study. For these measurements uncertainty intervals are expected to be closer to ±5% of the amount present.

Accordingly, the error intervals reported in Table 9 were obtained by computing the maximum and minimum possible values for the diffusion coefficient through application of the Wagner/Li-Powell analysis to the extreme cases. This approach is shown graphically in Figure 44 below. Error curves, as defined by the error in the WDS measurements, are plotted above and below the measured data, thereby establishing intervals within which the analysis was carried out.

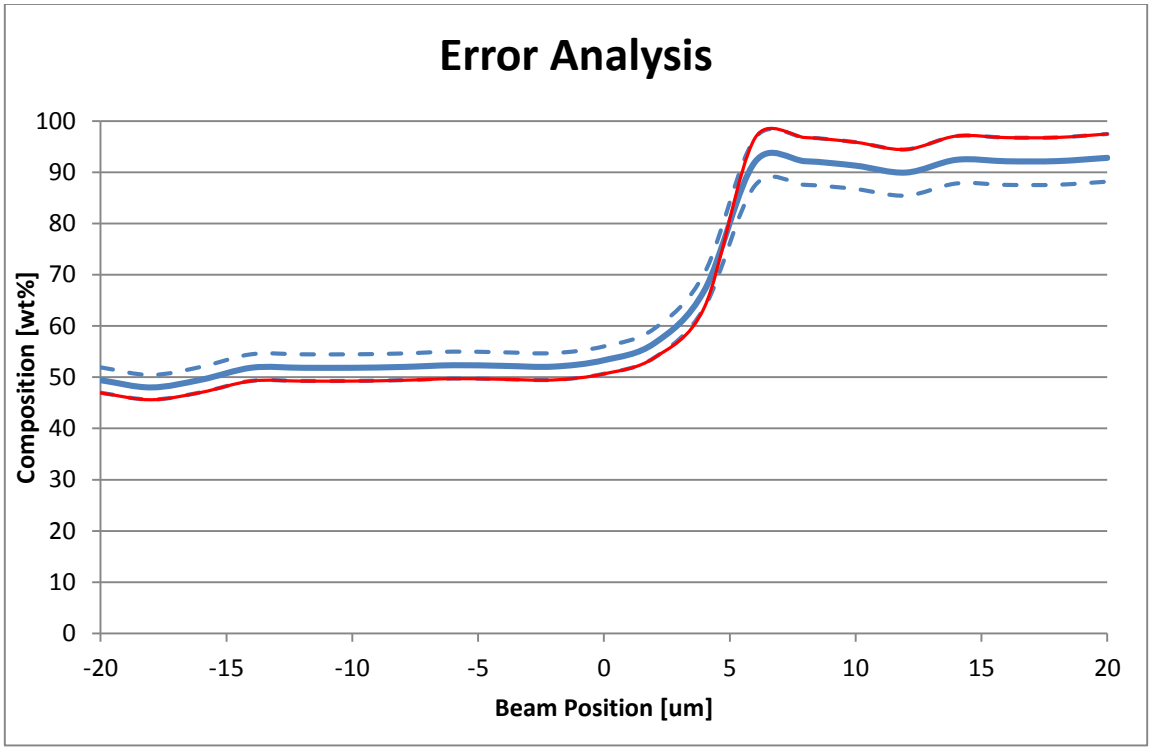

Figure 44: Procedure for calculating error in diffusion coefficient values from WDS measurement. Measured data is shown in blue, while error curves are shown dashed. In executing the Wagner/Li-Powell method, the maximum value of the diffusion coefficient, for example, is attained using the minimum composition values on the left side of the plot, and the maximum values on the right side; this example is shown in red. The procedure is vice versa for the minimum value of the diffusion coefficient.

Happily, almost all WDS measurements carried out in this study were observed to exhibit "good statistics", in that measured concentrations were well above the associated detection limits (measured values below the detection limit would, of course, be meaningless). In addition, totals of elemental concentrations at a given analysis point consistently were close to 100%, usually within about 2-3%, further validating the integrity of the data. These observations would seem to indicate that the WDS measurements were not a major source of error in this study.

However, quantification of uncertainty intervals due to the aforementioned causes for error in the previous section is much more tenuous. There was no way to assign a reliable uncertainly value to these factors, as there was too little information available as to if or how much they influenced WDS measurements. Put simply, there was too much uncertainty in the uncertainty. Consequently, it was not feasible to carry out any sort of meaningful analysis of the error induced by these factors, and they must simply be acknowledged as possible sources of some indefinite error.

5. SUMMARY AND CONCLUSIONS

In this study, atomic diffusion phenomena were examined in a metal-alloy nuclear fuel system. As can be seen in Table 9 (page 64) it was found that values of the diffusion coefficient, and therefore diffusion rates, were generally higher in the U-50Zr/Zr-10Gd system than in the U-50Zr/Zr-10Er system. It can therefore be concluded that the system which includes erbium is a more stable system, while that which includes gadolinium is a more mobile system. Also, diffusion occurred almost exclusively in one direction, from the displacer alloy into the fuel alloy, with very little diffusion in the other direction.

In addition, it was found that diffusion rates increased substantially at temperatures above the phase transformation from the δ phase to the γ phase. This is in agreement with what would be expected, as the more open BCC γ-phase structure would permit more mobility than the more closely-packed δ-phase structure. Different diffusion structures were observed to develop in the δ phase and the γ phase as well, as shown in Figure 35 (page 56).

In comparison to previous studies, the results of this work were fairly consistent with those found in existing literature. No previous work has been performed that examines the diffusion interactions of δ-phase U-Zr with erbium or gadolinium also present in the system; therefore, no direct comparisons could be made. Nevertheless, the δ-phase diffusion interfaces examined in this study were observed to develop a structure very similar in appearance to the δ-phase diffusion structure observed by Akabori, et al.,

as can be seen by comparing Figure 35(a) (page 56) and Figure 6 (page 11). Similarly, comparison of Figure 35(b) (page 56) and Figure 7 (page 12) demonstrates that the γ-phase diffusion structure, in accordance with the Gibbs Phase Rule, developed layers of intermetallic compounds with discreet compositions, as observed in the diffusion studies carried out by Huang, et al. Thus, the structures of the diffusion interfaces observed in this study seem to be in agreement with those observed in previous studies, albeit in different chemical systems.

As to the calculations of the diffusion coefficients carried out in this study, values were found to be significantly smaller than those found in previous studies. Recalling Table 2 (page 10), Akabori, et al. reported values of the diffusion coefficient in the δ-phase U-Zr system on the order of 10^{-17} to 10^{-18} m^2/s, approximately two orders of magnitude greater than those found in Table 9 (page 64). However, it should be recollected that the study carried out by Akabori, et al. did not include the burnable absorber elements, erbium and gadolinium; it is entirely possible that diffusion was suppressed by the presence of the lanthanides. It is also likely that diffusion was somewhat inhibited by the formation of stable metal oxides resulting from oxygen contamination; however, it is unclear as to how much each of these effects may have contributed to the repression of atomic diffusion. It is indeterminate whether the reduction of the values of the diffusion coefficients relative to those reported by Akabori, et al. is due mainly to the presence of the lanthanides, the presence of the oxides, some contribution from both, or other, unidentified factors.

In conclusion, the rate of atomic diffusion in the Lightbridge fuel system would seem to be sufficiently low that it is highly unlikely the effects thereof could be a limiting factor on fuel lifetime, or otherwise significantly inhibit fuel performance. Fission rates could be suppressed in the periphery of the fuel region due to burnable absorber diffusion into the fuel, since diffusion occurred predominantly from the displacer alloy into the fuel alloy; in contrast, however, fission heating in the displacer region is not expected to be significant, since very little diffusion occurred from the fuel alloy into the displacer alloy. In addition, diffusion interaction can be further reduced by selecting erbium as the burnable absorber species, rather than gadolinium. However, diffusion is greatly accelerated above approximately 600°C due to the phase transformation into the γ phase, and consequently diffusion phenomena could potentially become problematic if the fuel were to operate above this temperature threshold for a significant period of time. These findings conclude this study of atomic diffusion phenomena in a metal-alloy nuclear fuel system.

REFERENCES

Cited Works:

Akabori, M., Itoh, A., Ogawa, T., & Ogata, T. (June 1998). Interdiffusion in the U-Zr System at Delta-Phase Compositions. *Journal of Alloys and Compounds vol. 271-273*, 597-601.

Akabori, M., Itoh, A., Ogawa, T., Kobayashi, F., & Suzuki, Y. (June 1992). Stability and Structure of the Delta Phase of the U-Zr Alloys. *Journal of Nuclear Materials vol. 188*, 249-254.

Akabori, M., Ogawa, T., Itoh, A., & Morii, Y. (April 1995). The Lattice Stability and Structure of Delta-UZr2 at Elevated Temperatures. *Journal of Physics: Condensed Matter vol. 7*, 8249-8257.

Borg, R., & Dienes, G. (1988). *An Introduction to Solid State Diffusion.* Boston: Academic Press, Inc.

Callister, W., & Rethwisch, D. (2008). *Fundamentals of Materials Science and Engineering, 3rd Edition.* New York City: John Wiley & Sons.

Goldstein, J., Newburry, D., Joy, D., Lyman, C., Echlin, P., et al. (2003). *Scanning Electron Microscopy and X-Ray Microanalysis, 3rd Edition.* New York: Springer Science+Business Media.

Havela, L., Andreev, A., Goncalves, A., Sebek, J., Sechovski, V., et al. (2008). Crystal Structure and Electronic Properties of New Uranium Intermetallic Compound UGaZr. *Journal of Alloys and Compounds vol. 460 #1-2*, 83-89.

Huang, K., Park, Y., Ewh, A., Sencer, B., Kennedy, J., et al. (February 2012). Interdiffusion and Reaction Between Uranium and Iron. *Journal of Nuclear Materials vol. 424*, 82-88.

Landa, A., Soderlind, P., & Turchi, P. (December 2008). Density-Functional Study of the U-Zr System. *Journal of Alloys and Compounds vol. 478*, 103-110.

Li, G., & Powell, G. (1985). Theory of Reaction Diffusion in Binary Systems. *Acta Metallurgica vol. 33, #1*, 23-31.

Ogata, T., Akabori, M., Itoh, A., & Ogawa, T. (June 1996). Interdiffusion in Uranium-Zirconium Solid Solutions. *Journal of Nuclear Materials vol. 232*, 125-130.

Ogawa, T., Ogata, T., Itoh, A., Akabori, M., Miyanishi, H., et al. (June 1998). Irradiation Behavior of Microspheres of U-Zr Alloys. *Journal of Alloys and Compounds vol. 271-273*, 670-675.

Rothman, S. (May 1961). *Diffusion in Uranium, Its Alloys, and Compounds.* Argonne, Illinois: Argonne National Laboratory.

Wagner, C. (February 1969). The Evaluation of Data Obtained with Diffusion Couples of Binary Single-Phase and Multiphase Systems. *Acta Metallurgica vol. 17*, 99-107.

Other Reference Works, Not Explicitly Cited:

Dayananda, M. A. (September 1983). An Analysis of Concentration Profiles for Fluxes, Diffusion Depths, and Zero-Flux Planes in Multicomponent Diffusion. *Metallurgical Transactions vol. 14a*, 1851-1857.

Shatynski, S., Hirth, J., & Rapp, R. (April 1976). A Theory of Multiphase Binary Diffusion. *Acta Metallurgica vol. 24*, 1071-1078.

Zhang, D., McColl, I., & Wood, J. (1997). Diffusion Reactions in the Iron-Neodymium Binary Alloy System. *Philosophical Magazine vol. 75 #4*, 959-974.

APPENDIX A

This appendix provides the full content of the EES file that was developed to carry out thermal expansion calculations for the diffusion couple apparatus. An appropriate input value for the thickness of the zirconium buffer (highlighted in yellow) was found such that the resulting stress in the tie-bolts (the boxed result) was within the acceptable range.

Input:

```
cte_flanges=18.7e-6 [C^-1]
t_flanges=6.5 [mm]
cte_samples=7.2e-6 [C^-1]
t_samples=1.5 [mm]
cte_ta=6.8e-6 [C^-1]
t_ta=0.2 [mm]
delta_T=600 [C]
delta_flanges=cte_flanges*t_flanges*delta_T
delta_samples=cte_samples*t_samples*delta_T
delta_ta=cte_ta*t_ta*delta_T
delta_stack=2*delta_flanges+3*delta_samples+3*delta_ta+delta_buffer
t_bolts=2*t_flanges+3*t_samples+3*t_ta+t_buffer
cte_bolts=11.6e-6 [C^-1]
delta_bolts=cte_bolts*delta_T*t_bolts
epsilon_bolts=(delta_stack-delta_bolts)/(t_bolts+delta_bolts)
E_bolts=200e3 [MPa]
sigma_bolts=E_bolts*epsilon_bolts
cte_buffer=7.2e-6 [C^-1]
t_buffer=10 [mm]
delta_buffer=cte_buffer*t_buffer*delta_T
```

Results:

Unit Settings: SI C kPa kJ mass deg

cte_{bolts} = 0.0000116 [C^{-1}]	cte_{buffer} = 0.0000072 [C^{-1}]	$cte_{flanges}$ = 0.0000187 [C^{-1}]	$cte_{samples}$ = 0.0000072 [C^{-1}]
cte_{ta} = 0.0000068 [C^{-1}]	δ_{bolts} = 0.1956 [mm]	δ_{buffer} = 0.0432 [mm]	$\delta_{flanges}$ = 0.07293 [mm]
$\delta_{samples}$ = 0.00648 [mm]	δ_{stack} = 0.2109 [mm]	δ_T = 600 [C]	δ_{ta} = 0.000816 [mm]
ε_{bolts} = 0.0005433	E_{bolts} = 200000 [MPa]	σ_{bolts} = 108.7 [MPa]	t_{bolts} = 28.1 [mm]
t_{buffer} = 10 [mm]	$t_{flanges}$ = 6.5 [mm]	$t_{samples}$ = 1.5 [mm]	t_{ta} = 0.2 [mm]

APPENDIX B

This appendix provides all of the composition profiles collected in this study. Plots are superimposed over the corresponding BSE image of the region, at a 1:1 scale. The middle (50%) composition line in the plot is positioned at the approximate location that the WDS line scan was performed. The following pages contain a total of 12 composition profiles, one for the U-50Zr/Zr-10Er system and one for the U-50Zr/Zr-10Gd system in each of the six samples (the 8wk600 sample and 4wk650 sample are excluded since the diffusion interfaces separated).

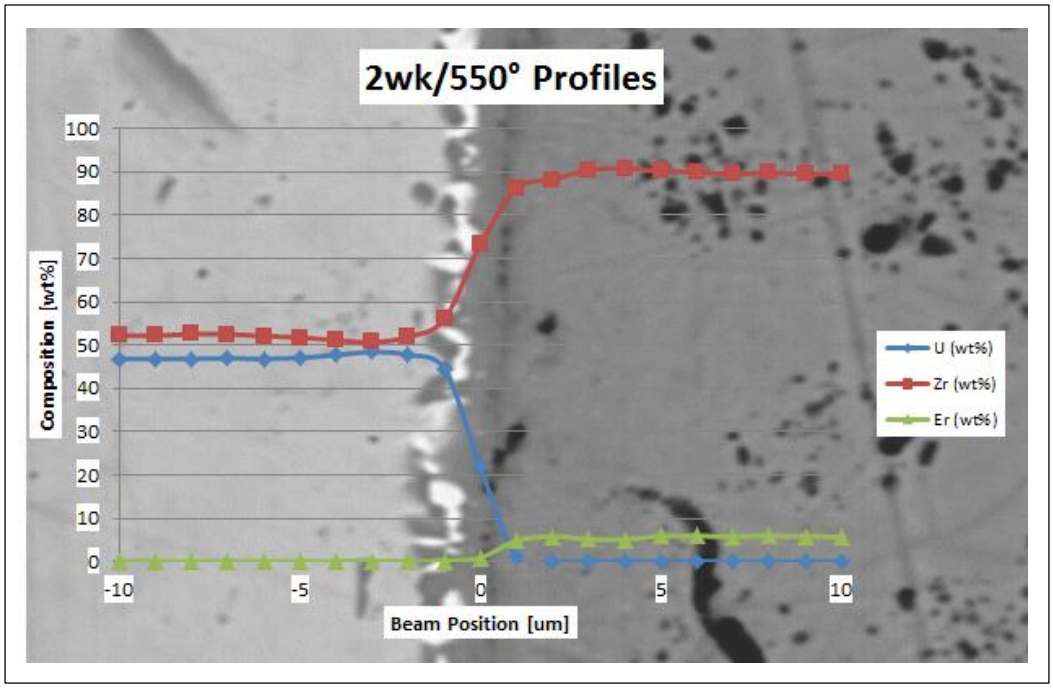

Figure 45: Composition profiles for 2wk550 sample, U-50Zr / Zr-10Er system.

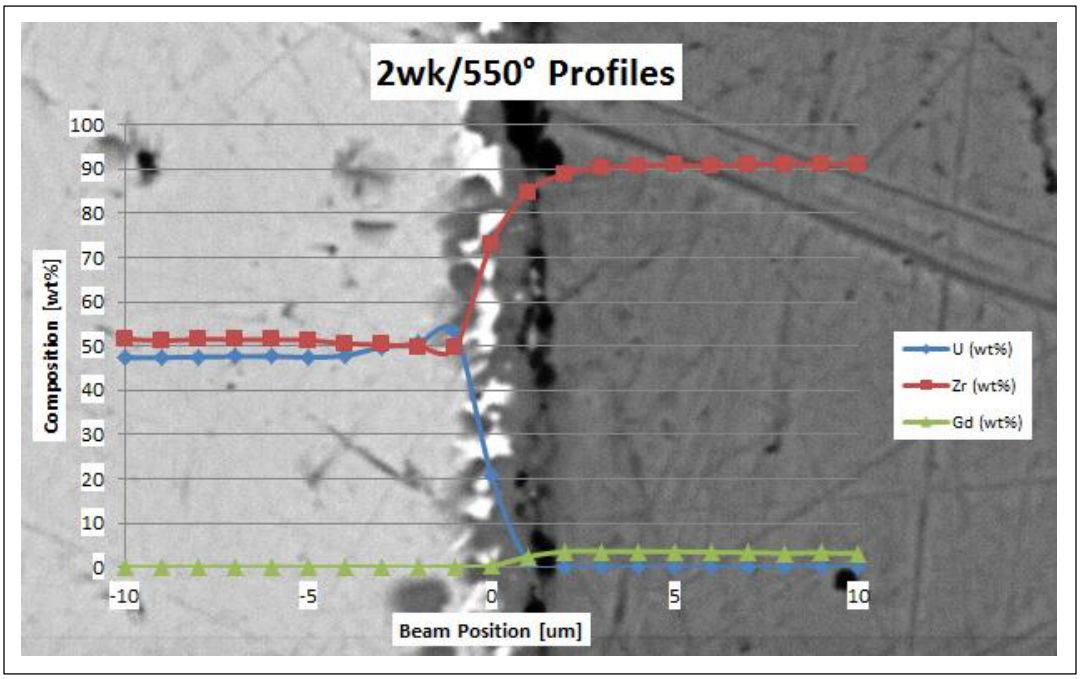

Figure 46: Composition profiles for 2wk550 sample, U-50Zr / Zr-10Gd system.

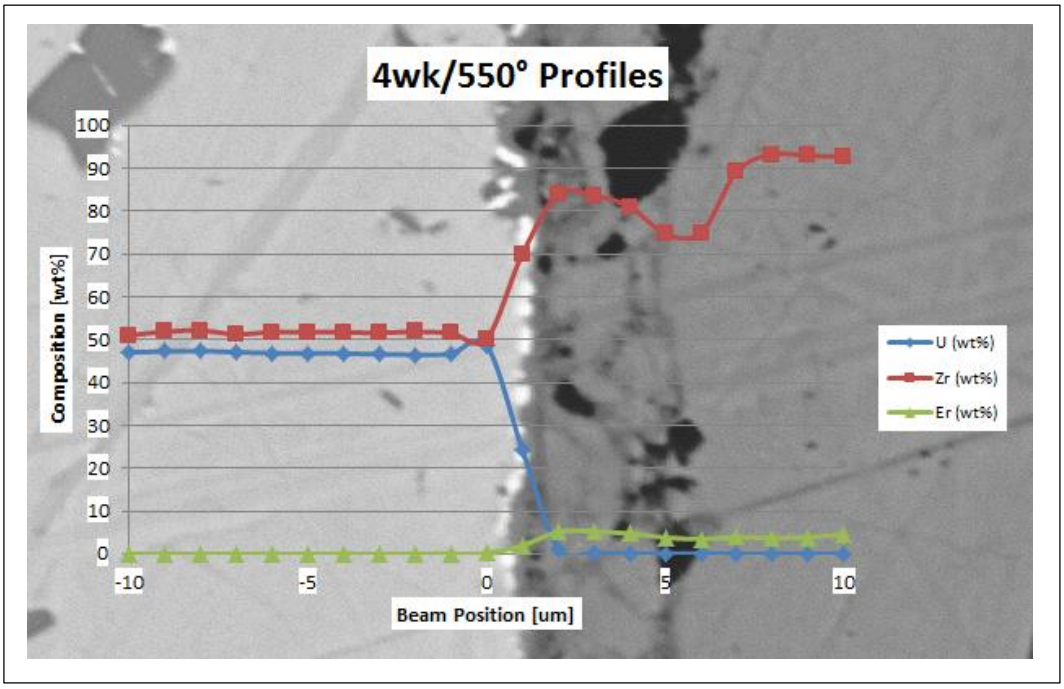

Figure 47: Composition profiles for 4wk550 sample, U-50Zr / Zr-10Er system.

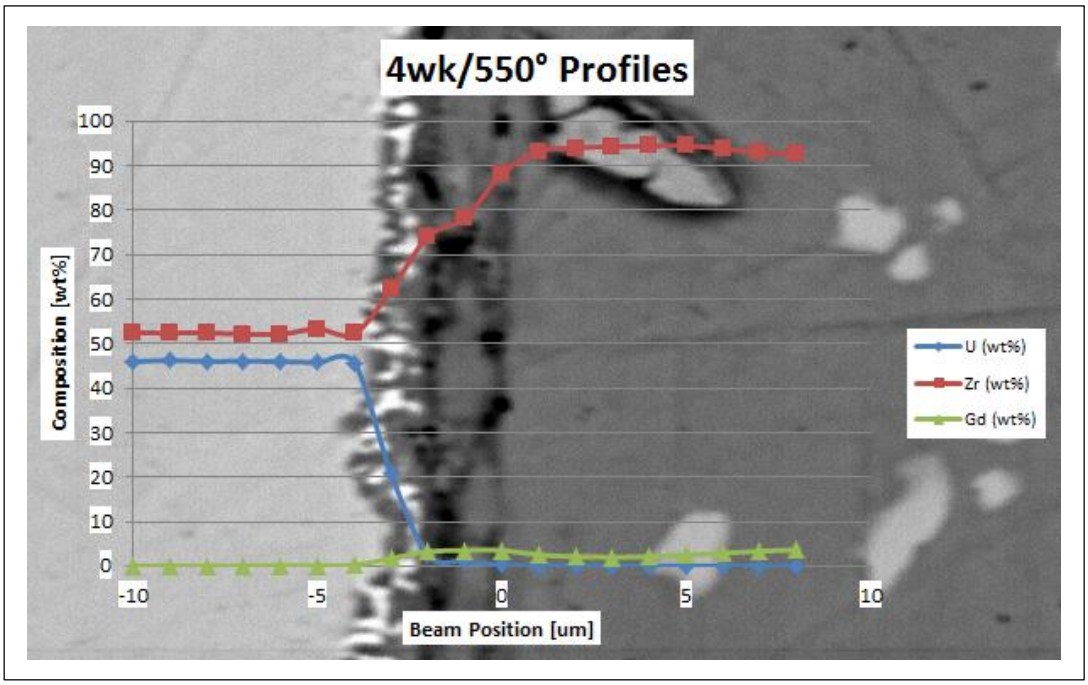

Figure 48: Composition profiles for 4wk550 sample, U-50Zr / Zr-10Gd system.

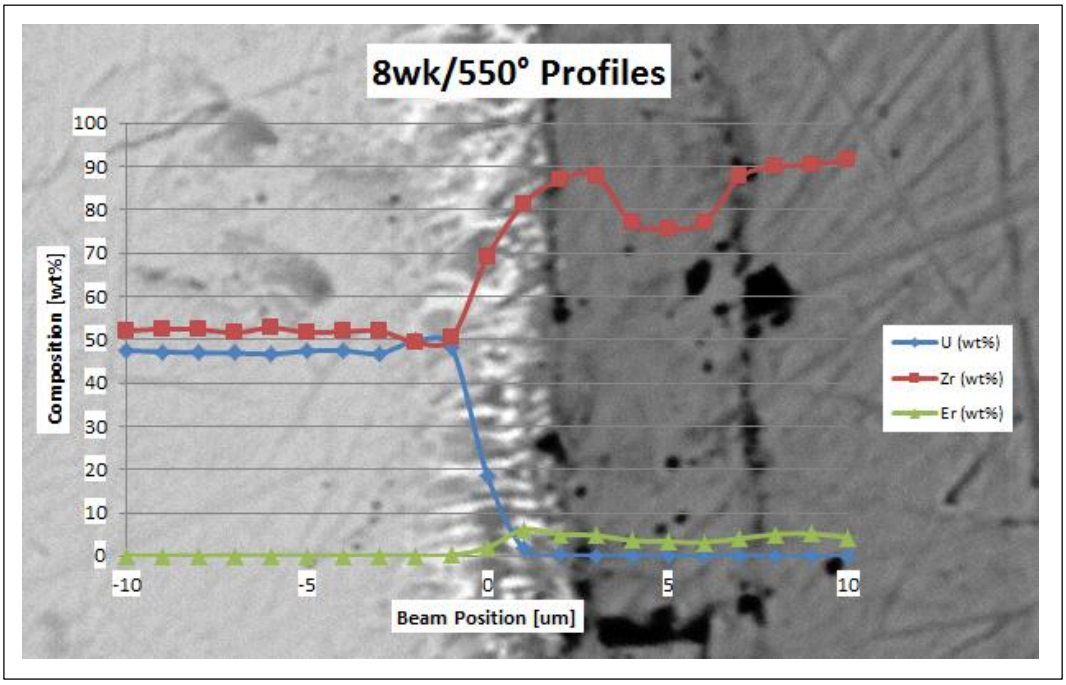

Figure 49: Composition profiles for 8wk550 sample, U-50Zr / Zr-10Er system.

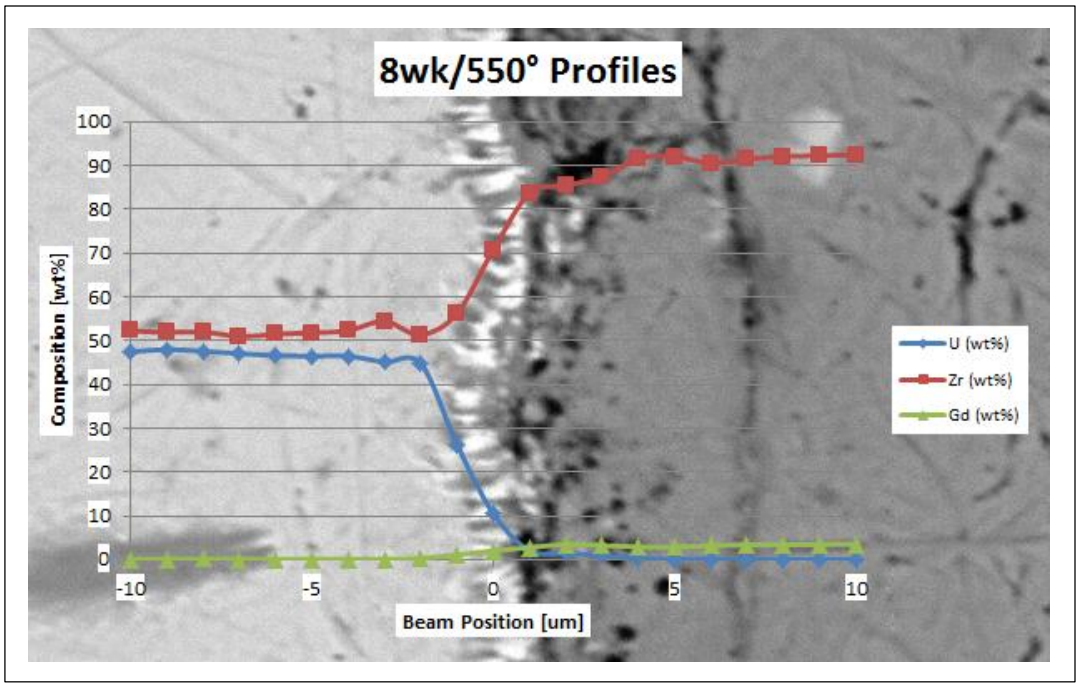

Figure 50: Composition profiles for 8wk550 sample, U-50Zr / Zr-10Gd system.

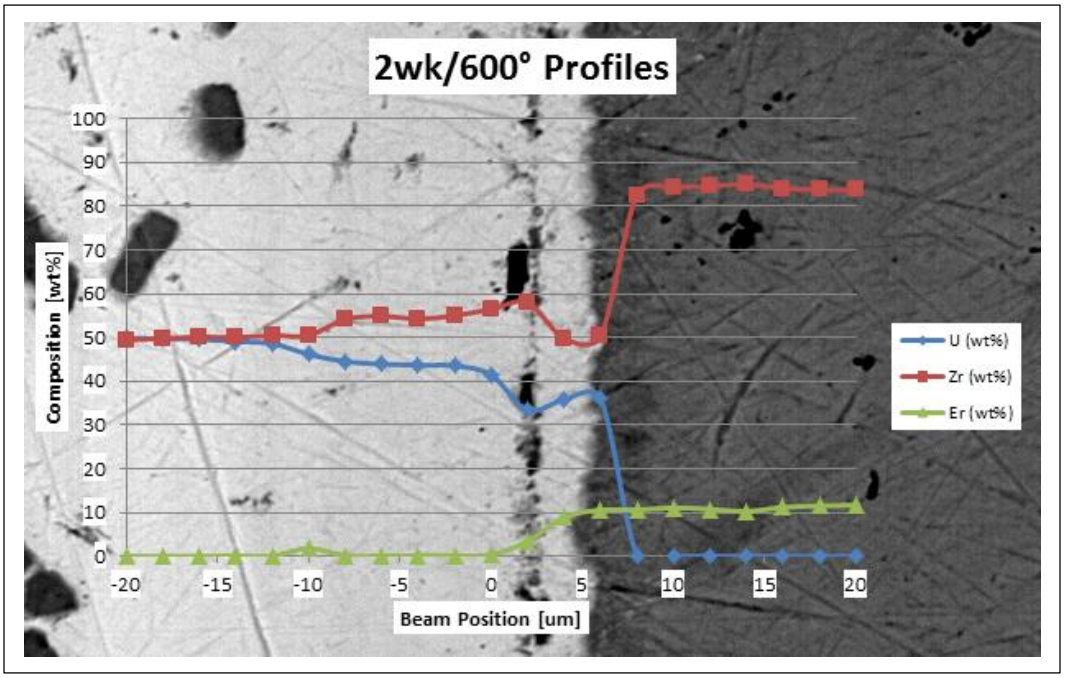

Figure 51: Composition profiles for 2wk600 sample, U-50Zr / Zr-10Er system.

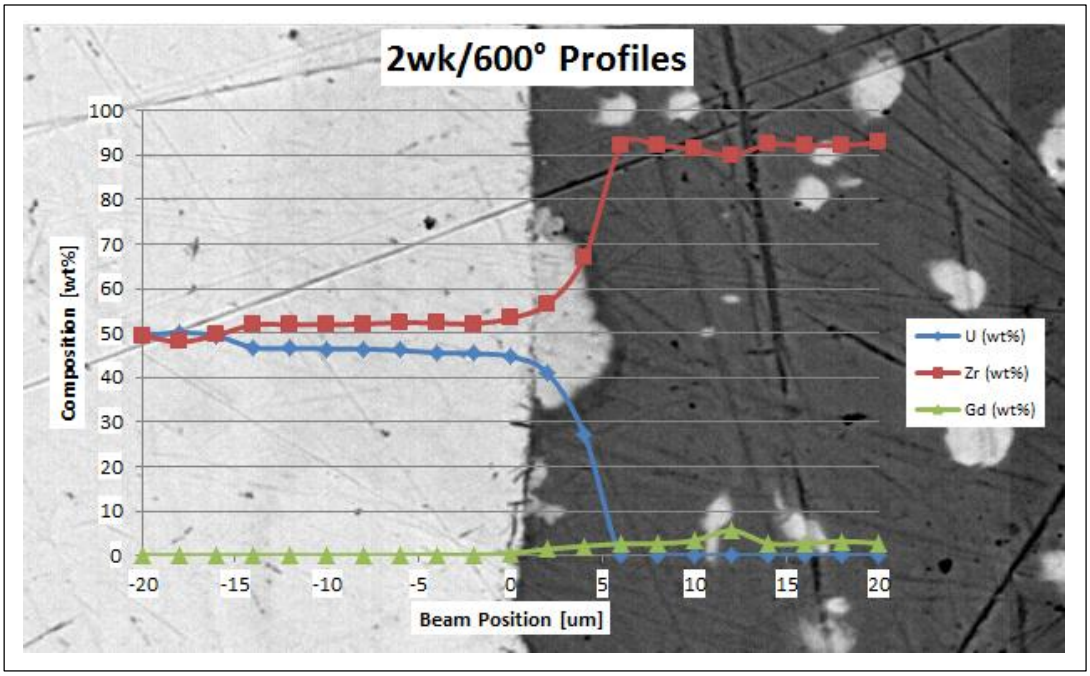

Figure 52: Composition profiles for 2wk600 sample, U-50Zr / Zr-10Gd system.

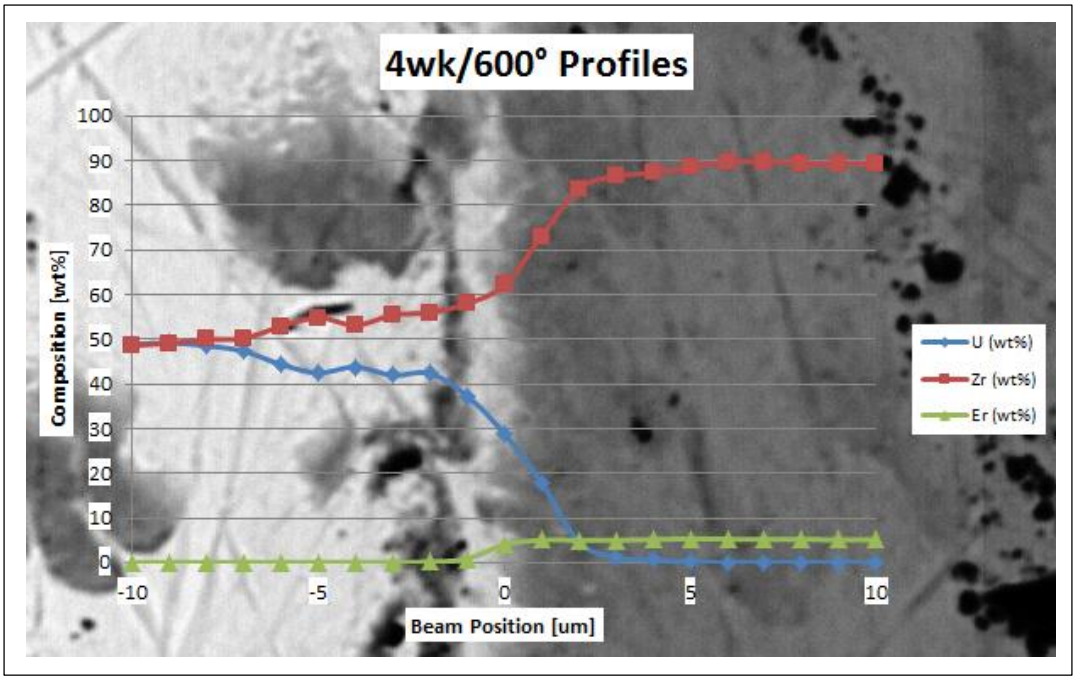

Figure 53: Composition profiles for 4wk600 sample, U-50Zr / Zr-10Er system.

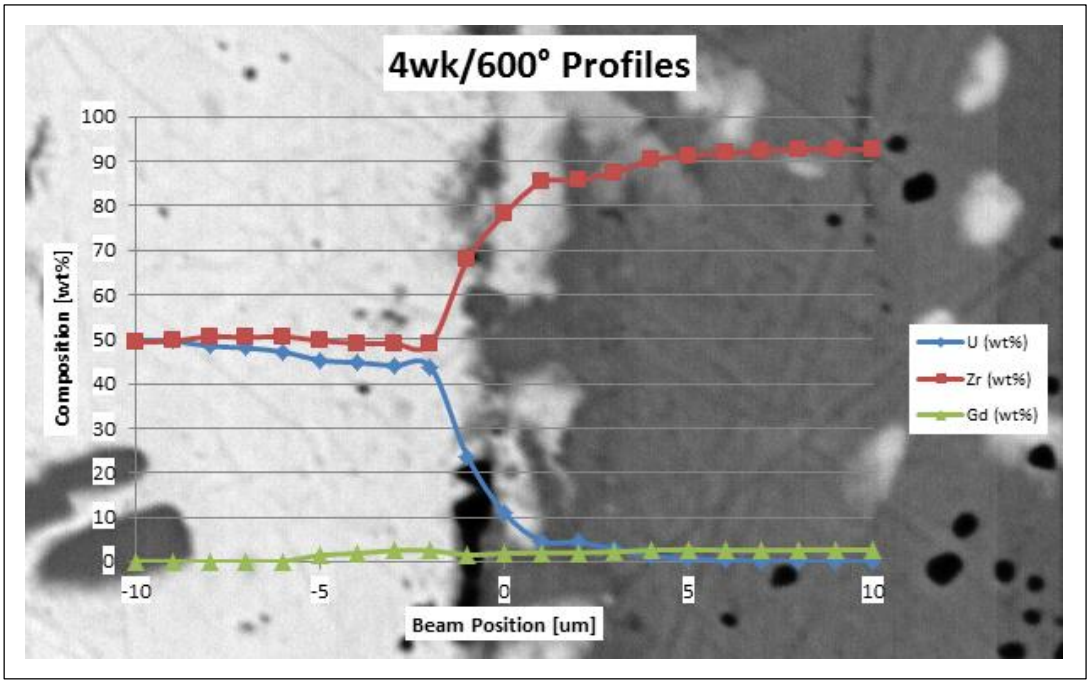

Figure 54: Composition profiles for 4wk600 sample, U-50Zr / Zr-10Gd system.

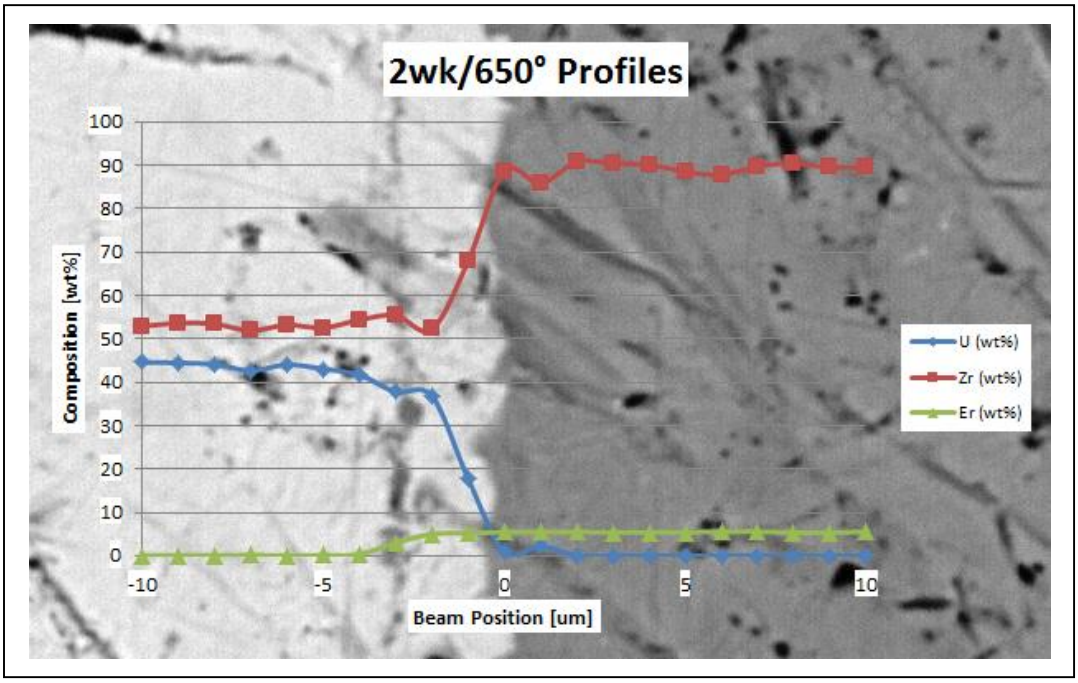

Figure 55: Composition profiles for 2wk650 sample, U-50Zr / Zr-10Er system.

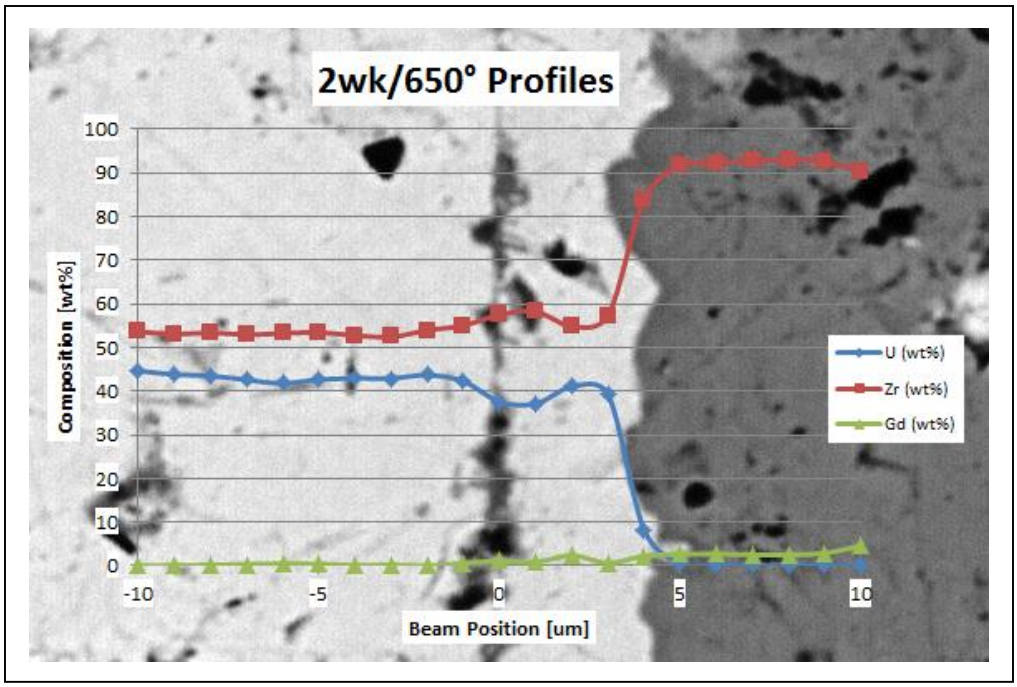

Figure 56: Composition profiles for 2wk650 sample, U-50Zr / Zr-10Gd system.

APPENDIX C

This appendix provides all of the oxygen concentration profiles generated in this study. It should be emphasized that these profiles are *qualitative only*; for the reasons discussed in Section 3.5.4 of this document, rigorous quantitative data could not be attained for oxygen concentrations. Plots are shown below the corresponding BSE image of the region, at a 1:1 scale. Oxygen data was not collected for the samples annealed at 550°C; only beginning with the 600°C samples was this analysis carried out. Also, the 8wk600 and 4wk650 samples are excluded since the diffusion interfaces separated Therefore, the following pages contain a total of 6 oxygen profiles, one for the U-50Zr/Zr-10Er system and one for the U-50Zr/Zr-10Gd system in each of the three samples for which this analysis was performed.

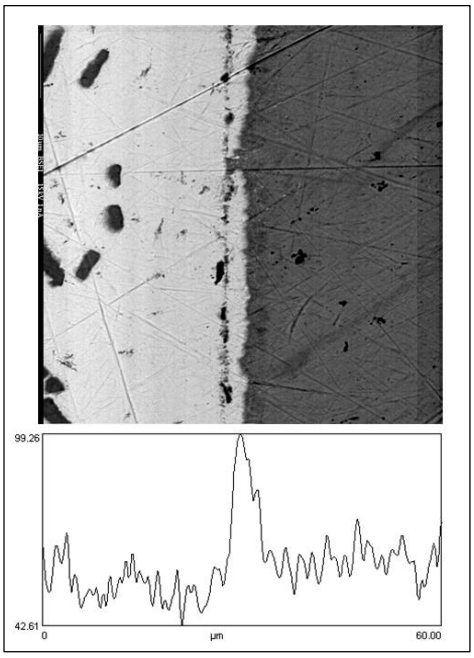

Figure 57: Qualitative oxygen profile for 2wk600 sample, U-50Zr / Zr-10Er system.

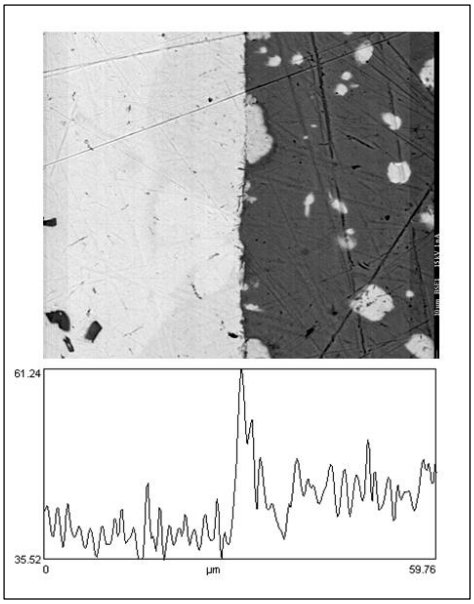

Figure 58: Qualitative oxygen profile for 2wk600 sample, U-50Zr / Zr-10Gd system.

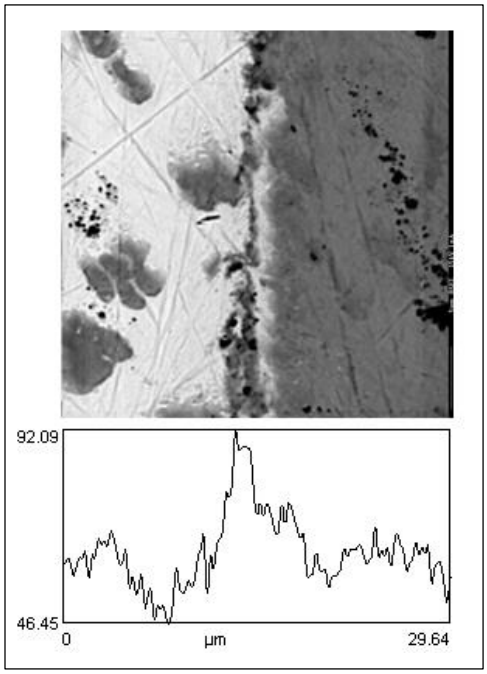

Figure 59: Qualitative oxygen profile for 4wk600 sample, U-50Zr / Zr-10Er system.

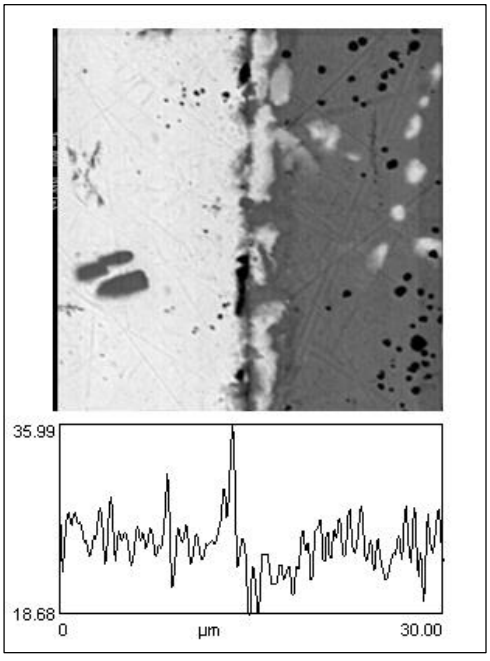

Figure 60: Qualitative oxygen profile for 4wk600 sample, U-50Zr / Zr-10Gd system.

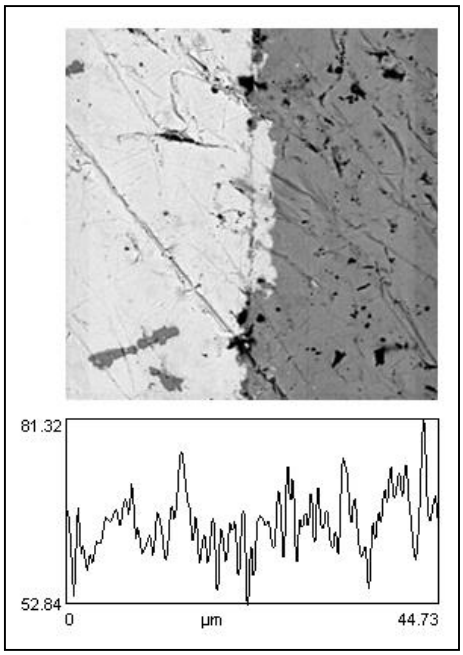

Figure 61: Qualitative oxygen profile for 2wk650 sample, U-50Zr / Zr-10Er system.

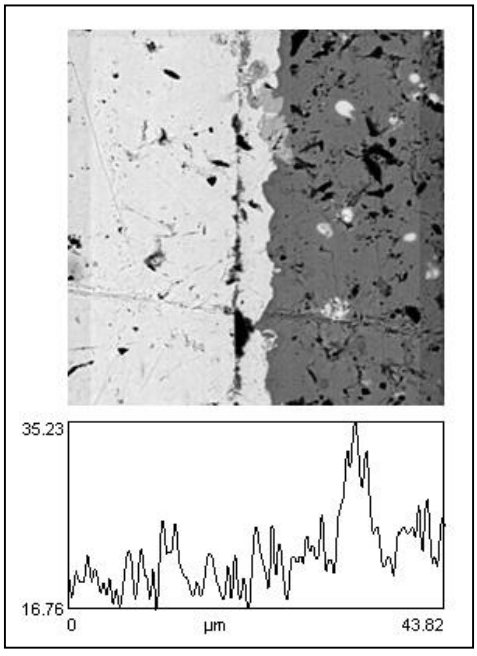

Figure 62: Qualitative oxygen profile for 2wk650 sample, U-50Zr / Zr-10Gd system.